Master of Science

# Synthesis and characterization of lithium vanadium borate composite as cathode materials for lithium-ion batteries by optimized sol-gel synthesis routine

The Graduate School of the University of Ulsan

Department of Chemistry

Minsoo Ji

# Synthesis and characterization of lithium vanadium borate composite as cathode materials for lithium-ion batteries by optimized sol-gel synthesis routine

Supervisor Professor Youngil Lee

A Dissertation

Submitted to

The Graduate School of the University of Ulsan

In partial fulfillment of the requirements

for the degree of

Master of Science

by

Minsoo Ji

Department of Chemistry

University of Ulsan, Ulsan, Korea

January 2019

# Synthesis and characterization of lithium vanadium borate composite as cathode materials for lithium-ion batteries by optimized sol-gel synthesis routine

This certifies that the dissertation of Minsoo Ji is approved.

Committee Chair Dr. Jiwon ha

Committee Member Dr. Jin-Chun Kim

Committee Member Dr. Youngli Lee

Department of Chemistry

Ulsan, Korea

January 2019

**Abstract**

$Li_3V_2(BO_3)_3$/C performed outstanding electrochemical performance when prepared with citric acid assisted sol-gel method. In order to optimize sintering temperature, we decided to range from 400 to 600 ℃ of sintering temperature via thermal analysis. As a result, material synthesized at 450 ℃ showed outstanding electrochemical performance. We investigated widely on physical and electrochemical properties of LVB/C as a new cathode material. LVB/C showed high discharge capacity 195.8 mAh $g^{-1}$ at 0.05 C-rate with a wide range voltage operability of 0.9 to 4.5 V. The present study will open new era for the novel poly-anion compound of $Li_3M_2(BO_3)_3$/C (M=Al, V, Cr, Fe, Ni and Ga) and $LiMBO_3F$ (M=Al, V, Cr, Fe, and Ga) based on triangular $(BO_3)^{3-}$ unit which is the lightest poly-anion group could enhanced the theoretical capacity and energy density and make low lattice volume change during lithiation / de-lithiation processes. This material has potential become promising cathode material and meet the stringent requirements of high theoretical capacity, wide voltage operability, low cost, safety and environmental friendliness for the application in hybrid electric vehicles (HEVs) and electric vehicles (EVs).

# 내용

## List of tables



## List of figures

NMR [5].

**Figure 2.4** Illustration of magic angle spinning (MAS). (a) A pair of nuclear spins I and S in the solid-state NMR sample tube rotate along the axis tilted magic angle (54.741°) with respect to the external magnetic field. (b) Rotation of the I–S internuclear vector under MAS is expressed by angles a (azimuth angle; rotation of I–S vector around the spinning axis) and b (polar angle; tilt angle between the I–S vector and spinning axis) [6,7]

**Figure 2.5** Spin-lattice relaxation ($T_1$) processes.[8]

**Figure 2.6** Transverse ($T_2$ and $T_2$*) relaxation processes[8].

**Figure 2.7** Schematic illustration of 1D NMR pulse sequence. (p1 = pulse width or duration, plw1 = RF field strength, aq = acquisition time and d1 = delay time)

**Figure 2.8** The spin-echo pulse sequence [9].

**Figure 2.9** $^{6}$Li MAS NMR spectra of the spinel $LiMn_2O_4$ based on sintering temperature [10].

**Figure 2.10** $^{7}$Li MAS NMR spectra of various $Li_xCoO_2$ ($0.33 < x < 1$) deintercalated phases recorded with a single-pulse sequence at 13 kHz spinning speed and the spinning sidebands are marked with asterisks (*) [11].

**Figure 2.11** (a) $^{7}$Li MAS NMR spectra of $LiFePO_4$ ($1^{st}$) and biphasic $Li_{0.5}FePO_4$ ($0.5LiFePO_4$:$0.5FePO_4$) ($2^{nd}$). (b) Deconvolution of biphasic $Li_{0.5}FePO_4$ with MAS =

**Figure 4.2** SEM image and the corresponding EDS elemental mapping of the $Li_3V_2(BO_3)_3$/C prepared by solid-state method (a) SEM image, (b) V, (c) O and (d) B elements.

**Figure 4.3** SEM image and the corresponding EDS elemental mapping of the $Li_3V_2(BO_3)_3$ prepared by oxalic acid assisted sol-gel method (a) SEM image, (b) V, (c) O and (d) B elements.

**Figure 4.4** SEM image and the corresponding EDS elemental mapping of the $Li_3V_2(BO_3)_3$/C prepared by citric acid assisted sol-gel method (a) SEM image, (b) V, (c) O and (d) B elements.

**Figure 4.5** Initial charge-discharge curves of $Li_3V_2(BO_3)_3$ composite prepared with (a) solid-state method, (b) oxalic acid assisted sol-gel method, and (C) citric acid assisted sol-gel method.

**Figure 4.6** (Ⅰ) Rate performance at various C-rate and (Ⅱ) long cyclabilities of $Li_3V_2(BO_3)_3$ composite prepared with (a) solid-state method, (b) oxalic acid assisted sol-gel method, and (C) citric acid assisted sol-gel method.

**Figure 4.7** DSC/TGA curves of precursor containing $LiNO_3$, $NH_4VO_3$, $H_3BO_3$, and citric acid

**Figure 4.8** The XRD patterns of $Li_3V_2(BO_3)_3$/C sintered at various temperature.
(a) 400 ℃, (b) 450 ℃, (c) 500 ℃, (d) 550 ℃ and (e) 600 ℃

**Figure 4.9** SEM images of $Li_3V_2(BO_3)_3$/C sintered at various temperature (from 400 to 600 ℃). Also, TEM images (a), (b) and (c) HR-TEM image of $Li_3V_2(BO_3)_3$/C

sintered at 450 ℃

**Figure 4.10** The XPS spectra of $Li_3V_2(BO_3)_3$/C. (a) Survey spectrum, (b) Lithium, (c) Boron, (d) Vanadium, (e) Carbon and (f) Oxygen.

**Figure 4.11** (Ⅰ) Rate performance and (Ⅱ) cycling cyclabilities of $Li_3V_2(BO_3)_3$/C sintered at various temperature. (a) 400 ℃, (b) 450 ℃, (c) 500 ℃, (d) 550 ℃ and (e) 600 ℃

**Figure 4.12** (a) charge and discharge curves and (b) cyclic voltammetry curves of $Li_3V_2(BO_3)_3$/C

**Figure 4.13** (I) $^{7}Li$ and (II) $^{51}V$ MAS NMR spectrum $Li_3V_2(BO_3)_3$/C at 25kHz. Isotropic peak is marked as arrow and the spinning sidebands are marked with asterisks (*).

## 1. Introduction of lithium ion battery

Many developments of renewable energy technologies that are contained solar cells, fuel cells, and biofuels and these technologies make more practical alternative energy [13]. The battery is known as energy storage device by converting electric energy with electrochemical reaction. In chemical batteries, a primary cell contained alkaline battery, magnesium battery and mercury battery are one that cannot easily be recharged after one use and are discarded following discharge. Most primary cells termed dry cells utilize electrolytes that are contained within absorbent material or a separator. On the other hand, a secondary cell can be electrically recharged by passing current through the circuit in the opposite direction to the current during discharge after initial charging and discharging.

A secondary cell consists of Ni-Cd battery, Ni-MH battery, lithium ion battery and Lithium ion polymer battery and the figure 1.1 is shown that there are some types of batteries. Among them, the development of lithium ion battery (LIB) is critical for advancements in a variety of applications ranging from individual electric products to hybrid electric vehicles. There are some advantages of lithium ion battery. Firstly, lithium ions have the lowest reduction potential compared as any elements and lithium ion-based batteries can have the highest cell potential. Also, lithium ions as light element have one of the smallest ionic radii of any single charged ion [14]. Secondly, it has high energy density and

reactivity and, it undergoes low self-discharge. However, it has some disadvantages that it is expensive and has a short life.

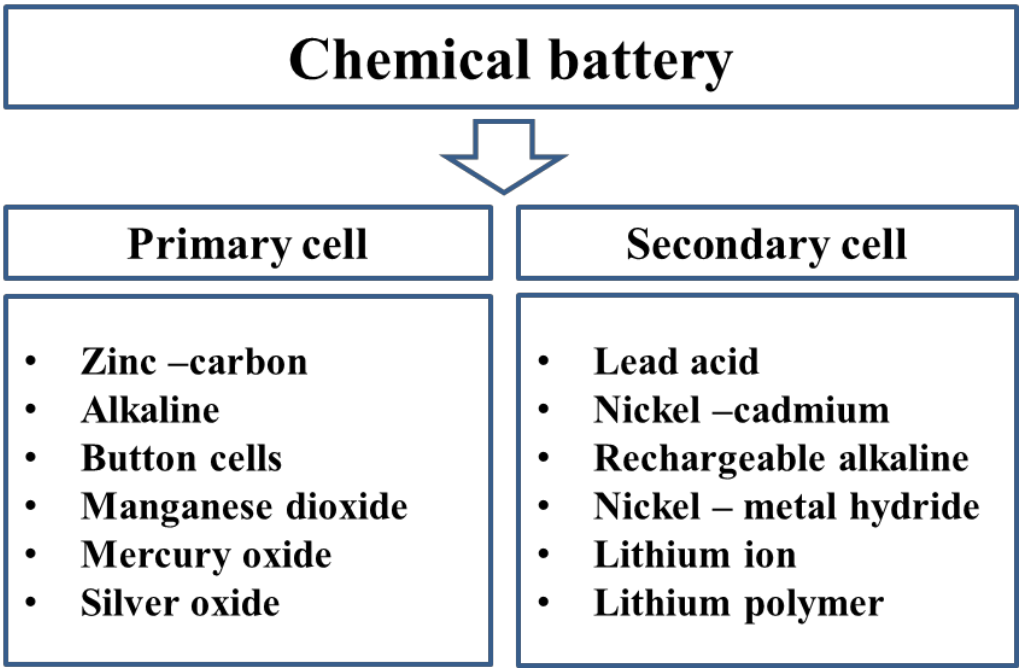


**Figure 1.1** Types of primary and secondary cell.

## 1.1 The principle of lithium ion battery

Lithium ion batteries (LIB) largely consist of cathode, anode, electrolyte and separator. Among cathode, Cathode materials include lithium-meal oxides such as $LiCoO_2$, $LiMn_2O_4$ and $LiFePO_4$. The most common cathode material is the layered $LiCoO_2$ are the most investigated materials for LIB and this material has high stability in the high voltage range. Anode materials include mainly graphite and lithium-metal. Electrolytes offer a high mobility for lithium ions and kinds is that liquid, polymer and solid-state electrolytes and lithium ions move through highly fine pores in separator separators that are used to retain safety and stability at high temperature for LIB. The figure 1.2 is shown that schematic diagram of charge-discharge process of lithium ion batteries [1].

There is $LiCoO_2$/graphite as an example of basic working on during the charge/discharge process to understand the basic principle of lithium ion battery. Lithium ions have mobility between the cathode and anode with the organic solvent as electrolyte and a separator in battery system which generally operates in higher working potential than 3 V vs. $Li^+/Li$. Reversible intercalation and deintercalation of lithium ions from typical structures is indicated in cathode and anode [15]. During the charging process, lithium ions are deintercalated from cathode materials structure and intercalated into graphite that is anode and lithium ions are transported in reverse direction on charging process. Cathode reveals oxidation and anode reveals reduction as electrochemical reaction on

discharge procedure and when the transition metal ion is reduced and accepts one electron, lithium is oxidized to lithium cation and loses electron on discharge. On this process, batteries with circuit convert chemical potential to electrical energy by electron flow called current [2].

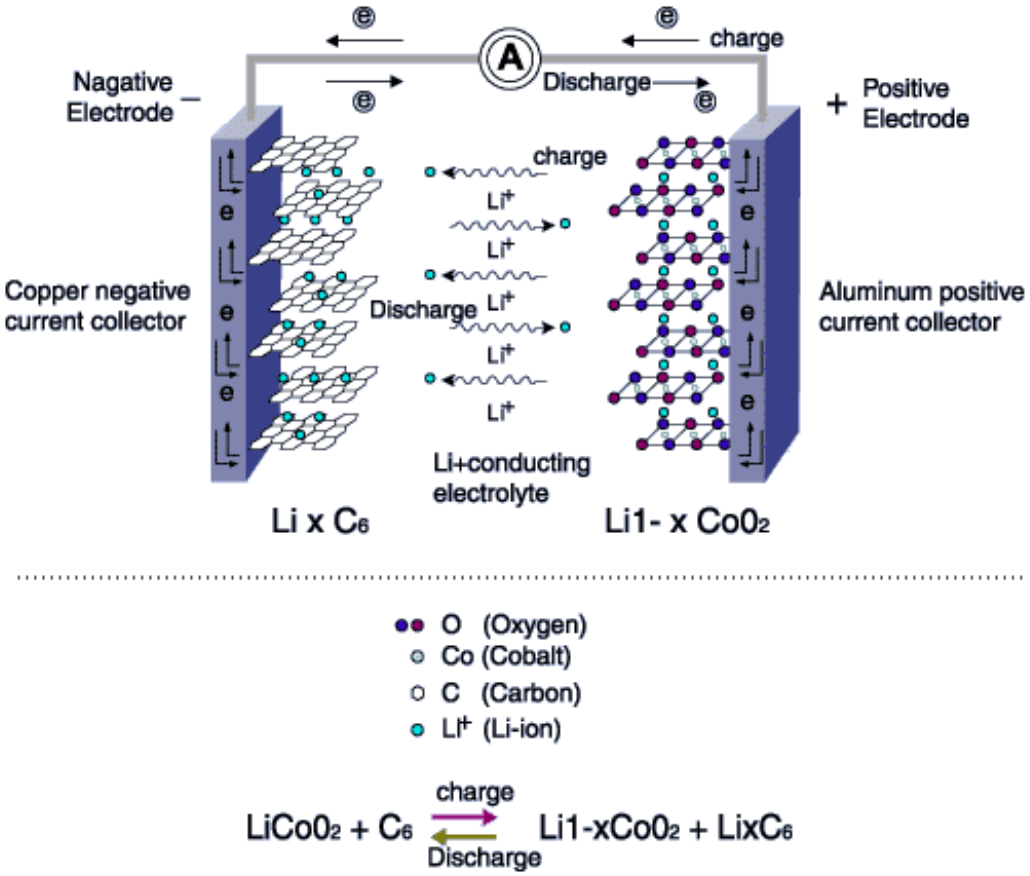


**Figure 1.2** Schematic diagram of charge-discharge process of lithium ion batteries [1].

## 1.2 Cathode materials for lithium ion battery

Among the component of LIB, cathode is a valuable part at life cycle ability, stability, reactivity and energy density and the typical cathode of LIB is composed of active materials and metal foil current collectors. The current collector acts as mechanical supports which can exist as electrode on battery and serves as electrical conductor which can connect electric energy that is made by chemical material of two electrodes into circuit. The aluminum metal foils are normally used as current collector for cathode due to their corrosion resistant caused by high oxidation state.

The electrochemical performance of LIB is related in structural character of cathode material. Cathode materials are largely divided into three types as structural character. The typical cathode materials of lithium ion batteries consist of layered lithium transition metal oxides $LiMO_2$ (M = Fe, Mn, Co, Ni, Ti, V, etc.), spinel lithium transition metal oxides, poly-anion compounds such as phosphates, silicates, fluorophosphates, fluorosilicates, borates [14].

The cathode material most commonly used in lithium ion batteries is $LiCoO_2$ [14,16]. Although $LiCoO_2$ has excellent properties of charge, discharge and high specific capacity whereas cobalt has toxicity and it is more expensive than other transition metals. Also, $LiCoO_2$ is not stable as compared to other potential electrode materials which undergoes performance degradation during

overcharging [17,18]. There are several reasons have been given for the degradation during cycling. The reason is that when the electrode is de-lithiated during charging, cobalt is dissolved in the electrolyte [19], thus less lithium ions can be intercalated during discharge. Also, the $CoO_2$ layer formed after full de-lithiation shears from the electrode surface [20], and less capacity for lithium intercalation is caused by that reason [14].

Another $LiMn_2O_4$ is contained material of lower cost, eco-friendly and more stable than $LiCoO_2$. However, it has a lower capacity than other cathode materials. This material is that in which phase changes can occur during cycling and the capacity has been due to loss of oxygen during charging and dissolution of manganese in the electrolyte [21]. On the other hand, there are a lot of interest has been directed to phosphate cathode material as poly-anion based compounds such as olivine structured $LiMPO_4$ (M =Fe, Mn, Ni, etc.), $LiVOPO_4$ and $Li_3V_2(PO_4)_3$ , which potentially allows for lower cost and high safety. A typical olivine cathode material has high stability due to strong covalent between phosphorus and oxygen atoms and it has low capacity fade after continuous cycle. So, it is widely used in lithium ion batteries and these have been characterized. However, $LiFePO_4$ has low electric conductivity ($10^{-9}$ S $cm^{-1}$) and lithium ion diffusion coefficient (D = $10^{-14}$ $cm_2$ $s^{-1}$). Also, it is suggested that olivine such as, $LiMnPO_4$, $LiCoPO_4$ and $LiNiPO_4$ does not have the excellent thermal stability compared as $LiFePO_4$.

Therefore, the relevant safety of phosphates is generally related to other poly-anion compounds which are a new material such as $Li_3V_2(PO_4)_3$ is a promising cathode material for lithium ion batteries.

The cathode material, $Li_3V_2(PO_4)_3$ with the high theoretical capacity of 197 mAh $g^{-1}$ has appeared as new promising cathode materials due to its enhanced electrochemical properties which is high Li diffusion coefficient, discharge voltage, and energy density [22]. This $Li_3V_2(PO_4)_3$ is observed as two different phases that are monoclinic and rhombohedral structure in which the monoclinic structure is more thermodynamic stable, and the rhombohedral structure indicate one plateau from one two-phase transition between $Li_3V_2(PO_4)_3$ and $Li_1V_2(PO_4)_3$ that corresponds to extraction of two lithium atoms [23]. The monoclinic structure that has all three lithium ions shows more complicated behavior from the series of two-phase transitions during lithium extraction. So, there are some advantages of monoclinic structured material are that it has high capacity and easy synthesis as a cathode material for LIBs. However, the rigid covalent bonding of larger poly-anion phosphate $(PO_4)^{3-}$ unit in (3D) framework of LVP assure the structural and thermal stability but the large poly-anion $(PO_4)^{3-}$ unit also bring some inactive mass into the electrode resulting in relatively low theoretical which lowers both the specific capacity and energy. So, the monoclinic $Li_3V_2(PO_4)_3$ has the low electronic conductivity ($2 \times 10^{-8}$ S $cm^{-1}$) to limit the wide application, several investigation to overcome this problem

have been made by addition of conductive materials [24].

For the improvements in electrochemical performance of $Li_3V_2(PO_4)_3$ (LVP), their isomorphs studies have been carried out such as surface conducting modification via coating of conducting metal oxides, various synthetic strategy, particle size reducing via formation of nanostructured materials, metal cation doping on lithium or iron sites, and anion doping at $(PO_4)^{3-}$ site to overcome these problems [25].

Considering the above mentioned issues, the evolution of borate compounds as cathode materials would be great of interest, as the $(BO_3)^{3-}$ unit is the lightest poly-anion group (M.W=58.8) among all poly-anion compounds of phosphate and silicates with larger tetrahedral $(PO_4)^{3-}$ unit (M.W=95.0) and heavier tetrahedral silicate $SiO_4$, could possibly increase the theoretical capacity, and energy density by approximately >1.3 times [26]. Additionally, the boron ion presents in $(BO_3)^{3-}$ unit show low transition metal redox energies which requires very small amount of lithium for reversibility involving the lowest volume change (ca. 2%) during cycling. The thermodynamic study of borates compounds shows the reduction couple between 3.1 V and 2.9V /Li with higher electronic conductivity ($3.9 \times 10^{-7}$ S/cm) [27] better than phosphate compounds which removes the obstacles of low $Li^+$ diffusivity, poor intrinsic electronic conductivity, high energy barrier in lithium ion channels and Li blockage by anti-site defects as reported in phosphate compounds. Recently, the successful establishment of very

few borate based compounds of $LiFeBO_3$ [28] and $LiMnBO_3$ [29] compounds as cathode material with the superior electrochemical performance. The poly-anion compound of $Li_3M_2(BO_3)_3$ (M=Al, V, Cr, Fe, Ni and Ga) based on triangular $(BO_3)^{3-}$ unit will be the promising cathode materials and meet the stringent requirements of high theoretical capacity, wide voltage operability, high energy density, long cycle life, superior electrochemical performance for the application in hybrid electric vehicles (HEVs) and electric vehicles (EVs).

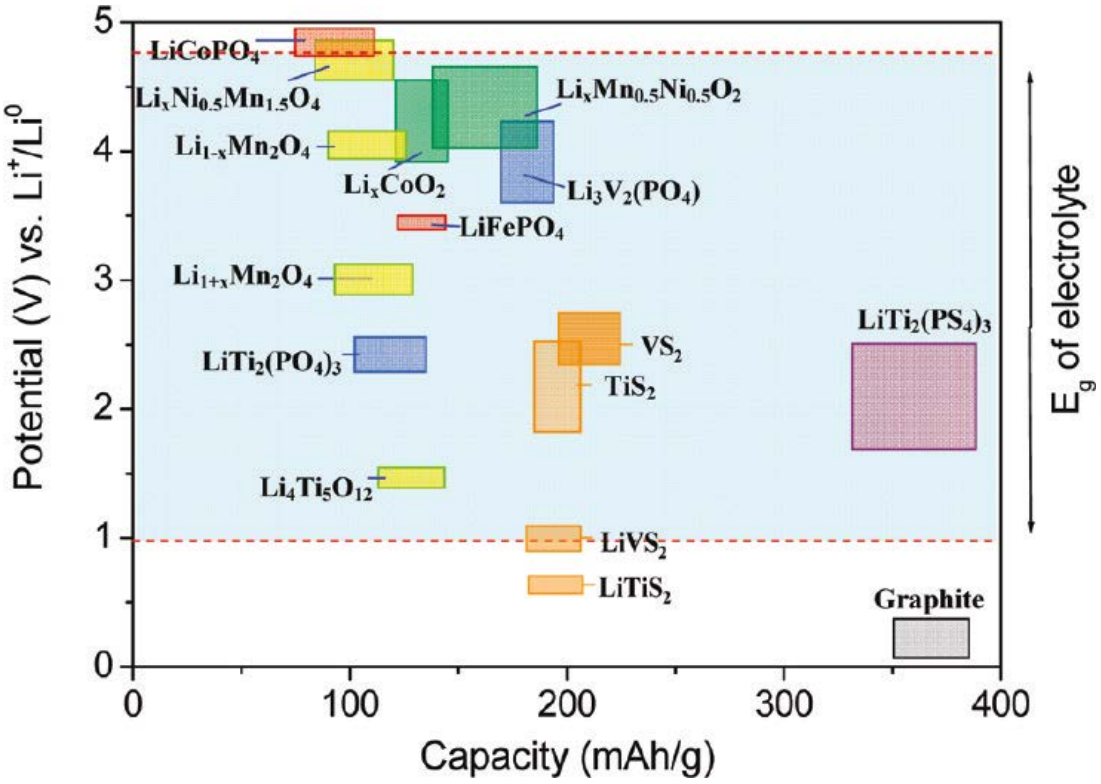


**Figure 1.3** Voltage versus capacity of several electrode materials relative to the window of the electrolyte 1M $LiPF_6$ in EC/DEC (1:1) [2].

| Material | **$LiCoO_2$** | **$LiMn_2O_4$** | **$LiFePO_4$** | **$Li_3V_2(PO_4)_3$** |
|---|---|---|---|---|
| Structure | Layered | Spinel | Olivine | Monoclinic, Rhombohedral |
| Potential vs. Li/Li+ | 3.9 V | 4.1 V | 3.5 V | 3.8 V |
| Specific capacity | 145 mAh $g^{-1}$ | 100 mAh $g^{-1}$ | 170 mAh $g^{-1}$ | 197 mAh $g^{-1}$ |
| Specific energy | 546 Wh $kg^{-1}$ | 410 Wh $kg^{-1}$ | 518 Wh $kg^{-1}$ | 550 Wh $kg^{-1}$ |

**Table 1.1** The comparison of the various sorts of typical cathode material

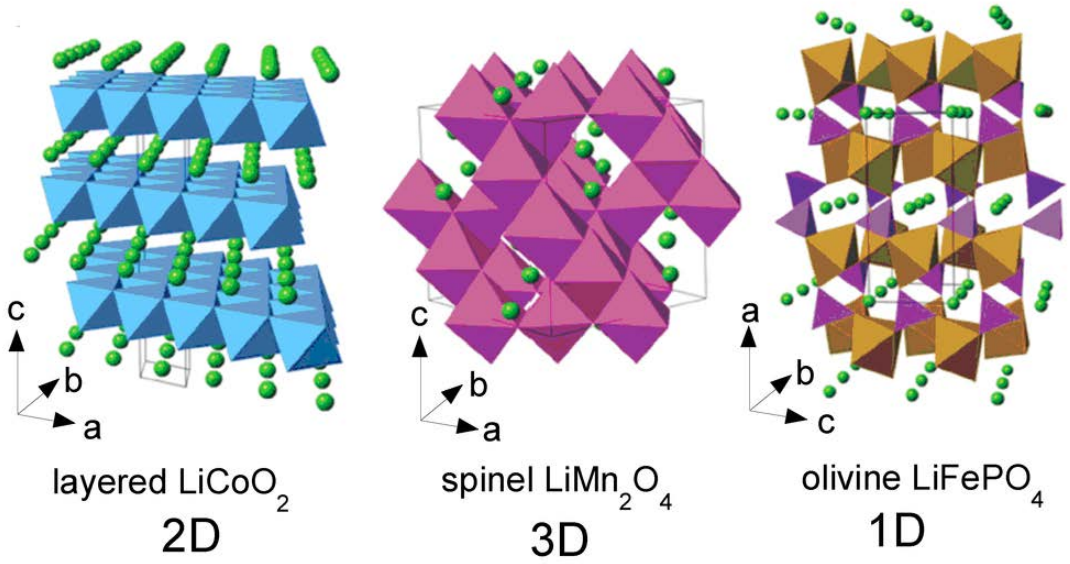


**Figure 1.4** Crystal structures of the three lithium-insertion compounds in which the $Li^+$ ions are mobile through the 2-D (layered), 3-D (spinel) and 1-D (olivine) frameworks [3].

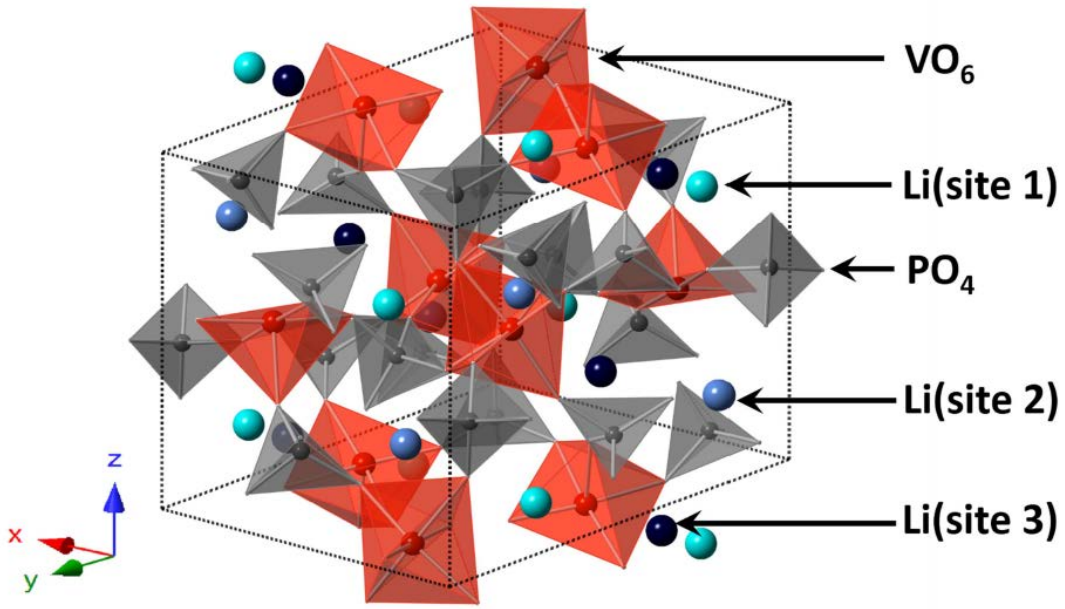


**Figure 1.5** Polyhedral representation of monoclinic $Li_3V_2(PO_4)_3$ [4].

## 2. Introduction of Nuclear Magnetic Resonance (NMR)

Firstly, the relationship between atoms, nuclei and molecules should be considered to understand Nuclear Magnetic Resonance (NMR). Each atom is composed of a positive charged nucleus having protons, neutrons and the nucleus is surrounded by negative charged electrons cloud. Molecules that are collections of bonded atoms are observed in a wide range of shapes and size from small compounds to larger compounds [30]. NMR is one of the well-known methods for identifying molecular structure. Also, the structure of proteins is very large, biologically important molecules for confirming the biochemical processes and these can be determined by NMR [30]. When sample is placed in a magnetic field, nuclei in the sample can absorb the specific energy at radiofrequency (RF) radiation. At that time, the nuclear magnetic resonance (NMR) can be used to observe structure of molecules. This energy at a specific resonance frequency is that depends on the strength of the magnetic field and the magnetic properties of the isotope of the atoms [9]. There are two general types of NMR spectrometers in use. Early NMR experiments were executed with a technique known as continuous wave (CW). When a constant magnetic field was maintained, the radio signal is monitored as scanning the frequency and brought each nucleus into resonance in sequence. After that, Fourier transform (FT) NMR is launched in the 1970s and this can convert signal to a frequency domain signal. At this present, FT-NMR is widely used in various application fields.

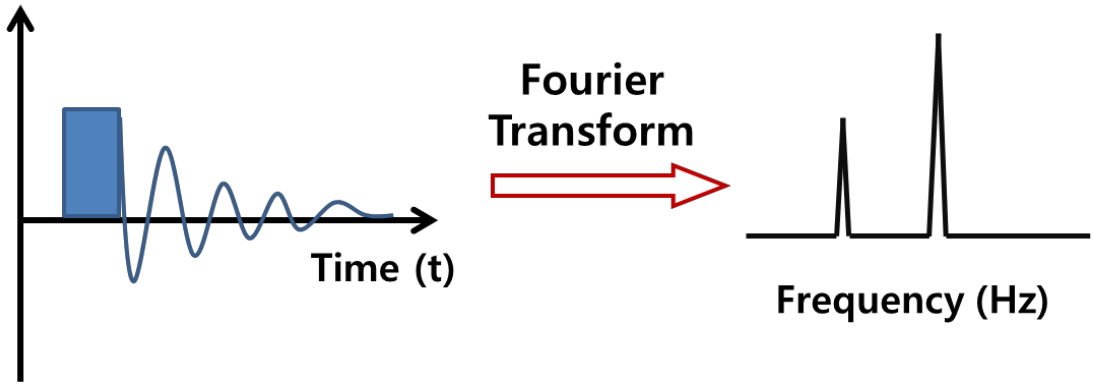


**Figure 2.1** Conversion from time domain to frequency domain using Fourier transform technique.

## 2.1 The principle of NMR

When the energy of photon corresponds to difference in energy between ground state and excited state, electromagnetic radiation is absorbed. Nuclear Magnetic Resonance (NMR) is related in this absorption phenomenon of electromagnetic radiation in the range of radio frequency (RF). RF radiation is enough to affect to nuclear spin of atoms and the orientation of spin axis can be changed by the absorption of radiofrequency radiation in magnetic field [31].

Nuclei with spin have angular momentum that is quantized. NMR activity occurs when nuclear spin quantum number ($I$) is not zero and it means that only a nucleus with an even atomic mass, odd atomic number or odd atomic mass has a nuclear spin. Thus, it can be measure in NMR. In case of $^{12}C$, $^{16}O$ is not available to measure because nuclear spin quantum number is zero and it means that the nucleus is not quantized. The angular momentum should be an integral or a half-integral since nucleus can have direction with (2I+1) discrete states. When a nucleus with a spin quantum number of 1/2 is put into external magnetic field ($B_0$), its magnetic moment becomes arranged in one of directions toward the field, depending on its magnetic quantum state [32]. In case of $^1H$ nucleus, it has two energy state since its nuclear spin quantum number is 1/2 (I = 1/2). Figure 2.2 illustrates that Zeeman Effect. When inserted in a magnetic field ($B_0$) nuclei that possess spin align themselves according to their energy states and this effect on their alignment is called the Zeeman Effect. A nucleus

with a magnetic moment in the same direction as the external magnetic field are in a low energy state and A nucleus with a magnetic moment in the opposite direction as the external magnetic field are in a high energy state.

When there is no external magnetic field, the nuclei are randomly oriented in any direction, but when a magnetic field ($B_0$) is applied, the nuclear spins are oriented in the same direction or in different directions. Therefore, energy becomes different. Spins in the same direction as the magnetic field ($B_0$) are more stable and exist in lower energy state ($\alpha$) and spins in the other direction are in a higher energy state ($\beta$). The number of nuclei in each spin state can be described by the Boltzmann distribution equation demonstrated on Equation 2.1. The Boltzmann equation expresses the relationship between temperature and the related energy as shown below.

$$\frac{N_\alpha}{N_\beta} = e^{-\Delta E/kT} \qquad \text{(Equation 2.1)}$$

Where $N_\alpha$ is the number of spins in the higher energy state, $N_\beta$ is the number of spin in the lower energy state, $k$ is Boltzmann's constant ($1.3804 \times 10^{-23}$ J $K^{-1}$), $T$ is the absolute temperature.

$$\Delta \mathrm{E} = \mathrm{hv} = \frac{\gamma \mathrm{h}}{2\pi} B_0 \qquad \text{(Equation 2.2)}$$

Substituting Equation 2.2 into Equation 2.1 gives

$$\frac{N_\alpha}{N_\beta} = e^{-\left(\frac{\gamma \mathrm{h} B_0}{2\pi k T}\right)} \qquad \text{(Equation 2.3)}$$

Where $N_\alpha$ and $N_\beta$ represent the population of nuclei in higher and lower energy states, E is the energy difference between the two spin states, k is the Boltzmann constant (1.3805x10-23 J· $K^{-1}$) and *T* is the temperature in K, h is plank's constant ( 6.626 × $10^{-34}$ J·s). At room temperature, the number of spins in the lower energy level is N lower whereas the number in the upper level is N upper. Spins of nucleus with a low energy state can be excited to a higher energy state, as irradiating the nucleus with electromagnetic radiation of the correct energy. The absorption of energy occurs during this transition [33]. Thus, the signal intensity of NMR increases is related with increasing the field strength.

| Isotope | Spin quantum number, I | Relative abundance in nature (%) | Gyromagnetic ratio, $\gamma^a$ |
|---|---|---|---|
| $^{1}H$ | 1/2 | 99.98 | 42.5759 |
| $^{13}C$ | 1/2 | 1.11 | 10.705 |
| $^{15}N$ | 1/2 | 0.36 | 4.315 |
| $^{19}F$ | 1/2 | 100 | 40.005 |

**Table 2.1** Magnetic properties of nuclei with spin quantum number of 1/2.

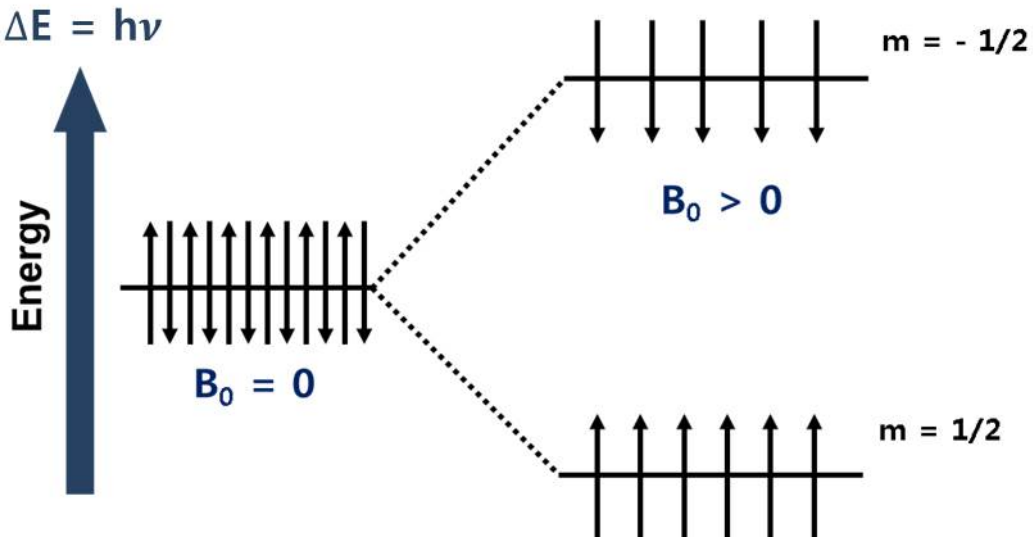


**Figure 2.2** Magnetic moments and energy levels for a nucleus with a spin quantum number of 1/2.

## 2.2 Solid-state NMR

Solution NMR to obtain a high-resolution spectrum refers to the case where the sample is in a liquid phase, and solid NMR refers to a case where it is experimented with a solid sample. Solid-state NMR instruments can measure samples in almost all states as well as in general solids. And in contrast to liquid samples that can use low power RF pulses, solid samples can detect spin interaction using a high-power RF pulse and can verify the physical properties of the sample but exhibit a broad spectrum due to the chemical shift anisotropy, dipole-dipole coupling and quadrupole coupling.

The electrons surrounding the nucleus shield the nuclei that are affected by the magnetic field and this is local fields caused by currents of electrons that are induced by the magnetic field $B_0$. The electron distribution around nucleus is asymmetric and the shielding effect depends on the orientation of the molecules under the influence of the magnetic field $B_0$. This called as chemical sift anisotropy and the resonance frequency depends on the orientation of chemical shift tensor that is affected with magnetic field. Nuclear spins exhibit a dipole moment that interacts with the dipole moment of other nuclei and it is called as dipole coupling. The intensity of the interaction is related in the spin species, the internuclear distance, and the orientation of the vector connecting the two nuclear spins with the external magnetic field $B_0$. Also, an atomic nucleus with a spin greater than 1 is split by the uneven electric field due to the quadrupole

moment and energy separation by quadrupole moments does not occur in the solution state due to the symmetry. Thus, quadrupole interaction is observed only in solid-state [33].

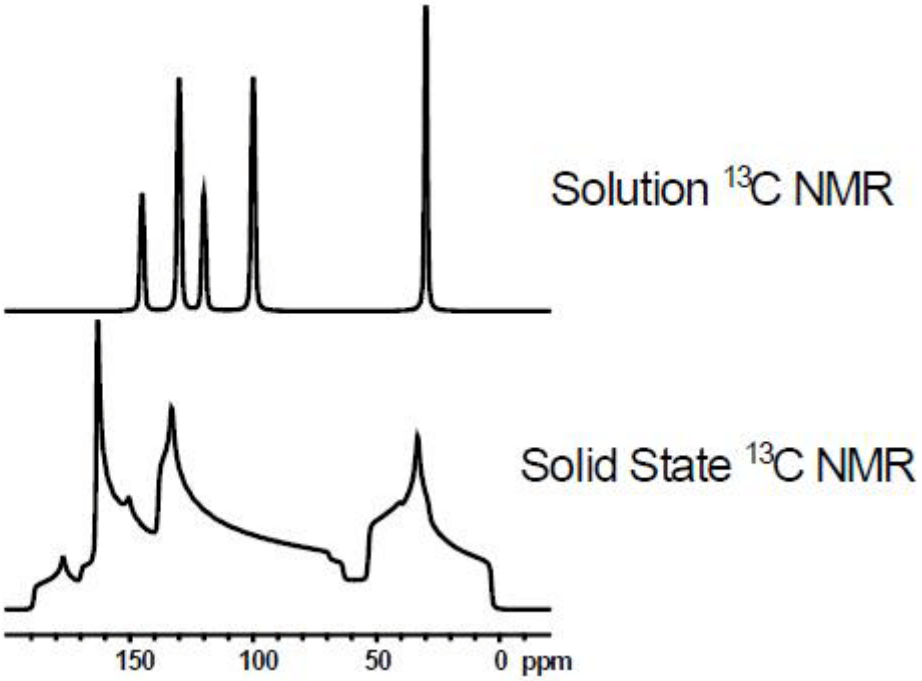


**Figure 2.3** Comparison between spectra of solution $^{13}$C NMR and solid state $^{13}$C NMR [5].

### 2.2.1 Magic Angle Spinning (MAS) technique

Unlike solution NMR, which puts a sample in a tube, solid NMR rotates from several kHz to tens of kHz using a rotor. Due to fast isotropic molecular tumbling, anisotropic interactions are averaged in solution NMR. However, broad peaks are observed due to chemical shift anisotropy, dipole-dipole coupling, and quadrupole interaction in solid. The chemical shift interaction is called the chemical shift anisotropy because of the anisotropy of the electronic environment that varies depending on the direction, which is caused by the surrounding electrons that modify the local environment of the nucleus. Also, dipolar interaction occurs by direct coupling spatially between nuclei and quadrupole interaction exists when the nuclear spin I is greater than 1/2 and is caused by the interaction between electric quadrupole moment of the nuclei and the asymmetric electric field gradients surrounding the nucleus. These three interactions include in the term of $3cos^2\theta - 1$ and when they are removed, sharp peaks appear. This technique is called Magic Angle Spinning (MAS) and the expression for the term to be 0 is as follows.

$$(3cos^2\theta - 1) = 0,\ \theta = 54.75°$$

And, the sample must be spin around an axis that is oriented at 54.74° with respect to the magnetic field $B_0$. The spinning speed must faster than the interaction strength to average out the anisotropy.

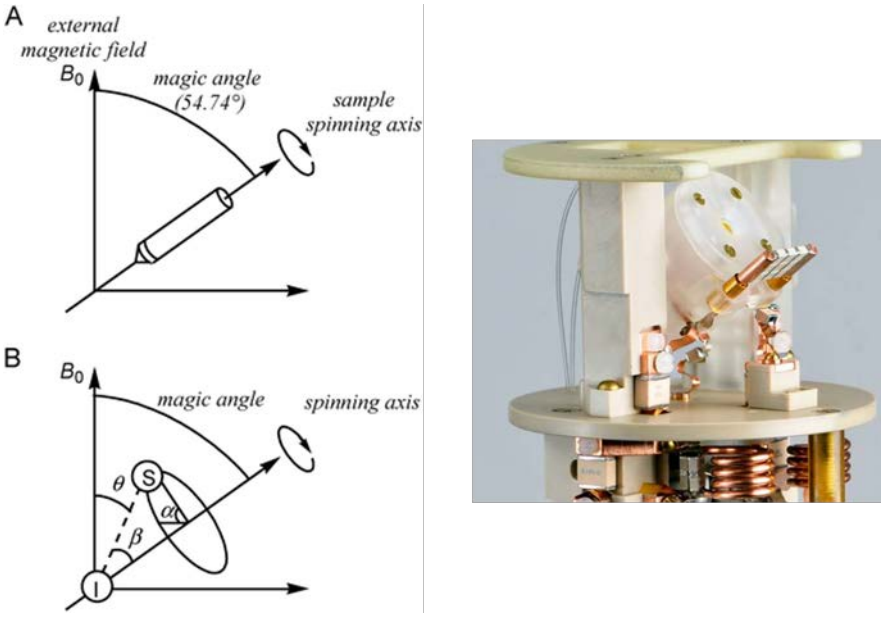


**Figure 2.4** Illustration of magic angle spinning (MAS). (a) A pair of nuclear spins I and S in the solid-state NMR sample tube rotate along the axis tilted magic angle (54.741°) with respect to the external magnetic field. (b) Rotation of the I–S internuclear vector under MAS is expressed by angles a (azimuth angle; rotation of I–S vector around the spinning axis) and b (polar angle; tilt angle between the I–S vector and spinning axis) [6,7]

### 2.2.2 $T_1$ (Spin-lattice relaxation) and $T_2$ (Spin-spin relaxation)

In NMR, a magnetic field generated by flowing an alternating current to a coil at armor frequency is called the $B_1$ magnetic field. When the alternating current flowing into the coil is turned on and off, a pulse $B_1$ magnetic field is

generated. The spin of the nucleus is aligned in the same or opposite direction to the external magnetic field along the z-axis. Since there are many nuclei oriented in the same direction as the magnetic field, net magnetization exists parallel to the external magnetic field.

At this time, the nucleus spin of the z-axis can be inverted to the x-y plane by injecting a short pulse. After the pulse injection, the spin system tries to return to equilibrium state, and the time taken for this is called the relaxation time. The relaxation time is divided into $T_1$ (Spin-lattice relaxation time) and $T_2$ (Spin-spin relaxation time) which indicates how fast the nucleus spins are magnetized in the z-axis. At equilibrium state, the net magnetization vector lies in the same direction as the external magnetic field ($B_0$) is called equilibrium magnetization ($M_0$).

When energy is applied to the system, the spin system is saturated and $M_z$ becomes zero ($M_z = 0$). In this saturation state, the time that it takes for $M_z$ to return to its original equilibrium state is called $T_1$ (spin-lattice relaxation time) and is expressed with the following equation and expressed as figure 2.5.

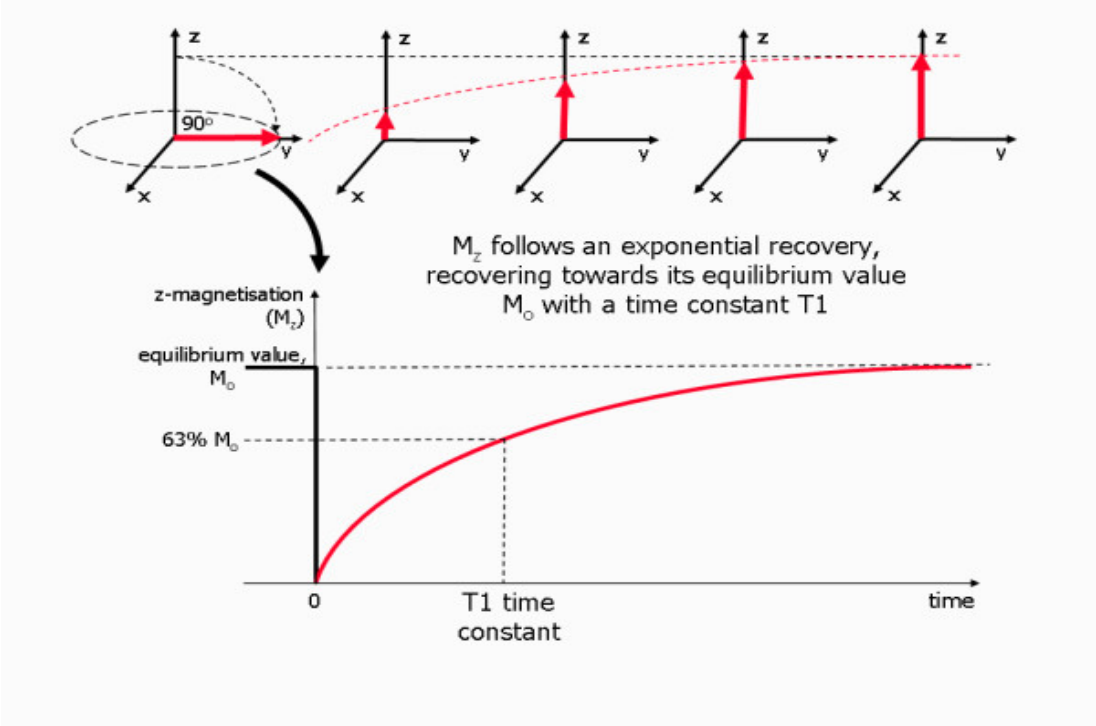


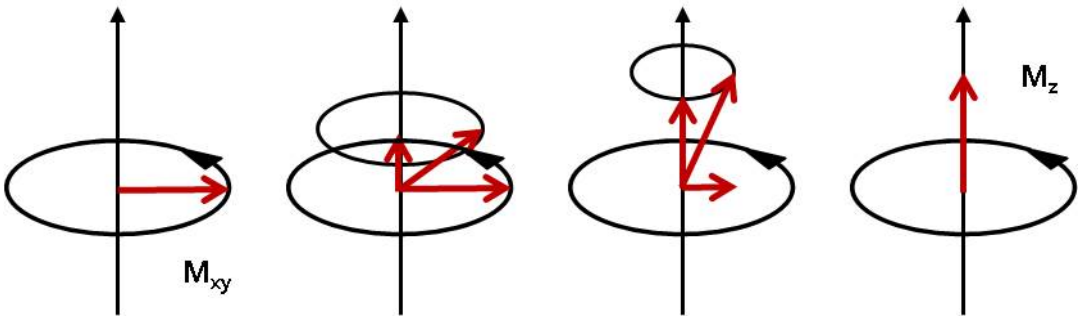


**Figure 2.5** Spin-lattice relaxation ($T_1$) processes.[8]

$$M_z = M_0 (1-e^{-t}/T_1) \qquad \text{(Equation 2.4)}$$

When the net magnetization lies in the x-y plane by a pulse, it rotates about the z-axis at the larmor frequency. The spinning motion is called precession. Precession and net magnetization experience slightly different magnetic fields in each spin, and eventually rotate at different larmor frequencies and dephasing begins to occur. As a result, a larger dephasing occurs over time. The time required for the transverse magnetization $M_{xy}$ to return to the equilibrium state is referred to as T2 (spin-spin relaxation time) and is represented by the following equation and expressed in figure 2.6.

$$M_{xy} = M_{xyo}\ e^{-t/T_2} \qquad \text{(Equation 2.5)}$$

That is, $T_1$ is the time for how fast the nuclear spins are magnetized in the z-axis, $T_2$ is how fast the magnetization is lost in the x-y plane, and $T_2$ is equal to or less than $T_1$.

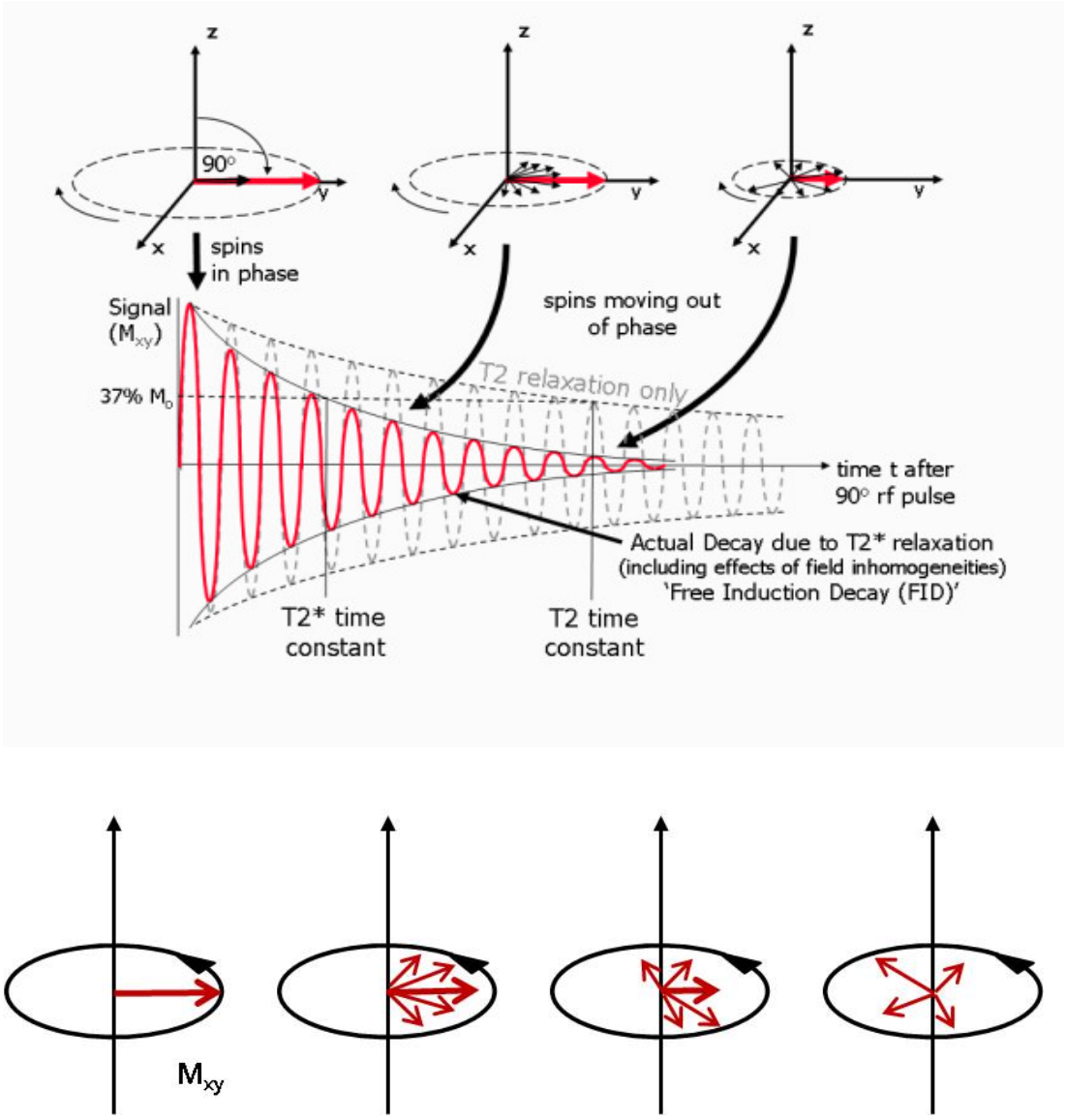


**Figure 2.6** Transverse ($T_2$ and $T_2$*) relaxation processes[8].

### 2.2.3 Spin echo pulse sequence (Hahn echo)

A radio pulse excites a relaxing nucleus while acquiring a signal. The signal is obtained by decreasing the dephasing after the net magnetization vector carries out a precession about the z-axis. At this time, a sine curve is obtained with exponential decay, which is called free induction decay (FID). The most commonly used pulses in NMR are 90° pulses and 180° pulses. The 90° pulse maximizes the signal to the x-y plane where the NMR signal can detect net magnetization in the z-axis. On the other hand, a 180° pulse reverses the density of the spin, although the NMR signal cannot be detected. The pulse sequence of 1D NMR is shown as follows.

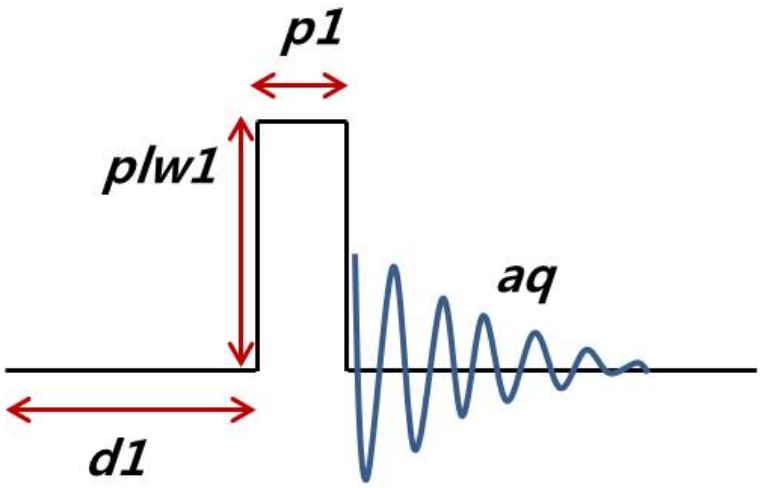


**Figure 2.7** Schematic illustration of 1D NMR pulse sequence. (p1 = pulse width or duration, plw1 = RF field strength, aq = acquisition time and d1 = delay time)

The parameters of spectrometer frequency, pulse width (pw), recycle delay (d1) and acquisition time (aq) are important to obtain NMR signals. The spectrometer frequency is a specific frequency of a radio wave pulse which depends on the strength of the magnetic field and the type of nucleus to be measured. The pulse width is the amount of time of the pulse energy applied to a particular sample to invert the spin in the x-y plane and depends on the power or attenuation of the pulse. The recycle delay (d1) appears at the beginning of the pulse sequence and is the time it takes for the spin to completely magnetize in the z-axis, also called delay time. After the radio wave pulse is applied, the nuclear spins do not immediately return to equilibrium and relaxes with time constant $T_1$. This depends on factors such as the nuclear environment, temperature, solvent, and other magnetic field conditions. Without sufficient relaxation time between pulses, the signal is reduced, and integration is not accurate. The specific time to obtain the FID is called acquisition time. If it is too long, the noise becomes large. If it is too short, a peak not related to the actual signal is observed [34].

The spin-echo pulse sequence in one of the pulse sequences most commonly used in NMR is intended to reduce any uneven effects due to spin relaxation and precession at different speeds in the sample. In solid NMR, it is mainly used for short $T_2$. After applying a 90° pulse, apply a 180° pulse and rotate the magnetization 180° about the x'-axis. This is for preventing the loss of

magnetization by applying a 180° pulse, which is an inversion pulse with a non-uniform phase of zero [35]. After a 90° pulse is applied, a 180° pulse is applied after a short time of τ and another time of τ, which is the same time that causes a spin echo signal. The signal thus obtained is called echo, not FID.

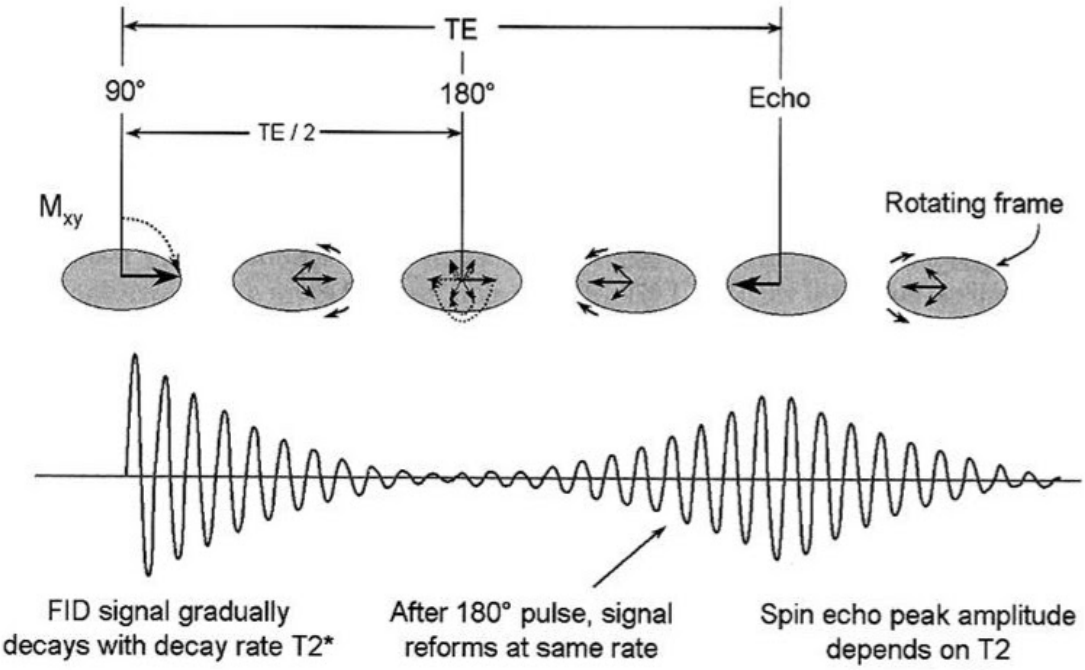


**Figure 2.8** The spin-echo pulse sequence [9].

### 2.2.4 Structural analysis using NMR for cathode materials

It is important to study structure measurement around lithium ion and the location and migration path of lithium ion among development factors of lithium ion battery.

Solid-state NMR is useful for analyzing the bonding structure between lithium ions and transition metal oxides in a cathode material. The NMR spectra are heavily influenced by the electrical structure of the material, and it is possible to distinguish between diamagnetism and paramagnetism. Structural analysis is made mainly for pure materials, and it is possible to check how the structure of the local structure changes after several charges and discharges. As nuclear spins of $^{6}Li$ and $^{7}Li$ have more than one in solid-state NMR, the Li MAS NMR spectrum of the battery material is affected by large interactions including quadrupole coupling and interaction with unpaired electrons in paramagnetic samples. As a result, the signals can be very complex, but using the previously described MAS NMR, high resolution signals can be obtained by rotating the sample at a high spinning rate.

In the case of $LiM_2O_4$, which is a material of the spinel structure synthesized at 700 ° C, the manganese ion retains the spinel host framework as a whole while circulating from $LiM_2O_4$ to $MnO_4$, a large hyperfine shift of 500 ppm or more is confirmed from the chemical shift range of a typical lithium

containing diamagnetic compound in the $^{6}Li$ and $^{7}Li$ MAS NMR spectra. Also, this material is a mixture containing both $Mn^{3+}$ and $Mn^{4+}$ ions and is a hopping semiconductor that occurs between $e_g$ orbitals of manganese ions. Since this hopping time scale is faster than the NMR time scale, it appears that the spin of lithium is averaged to a manganese oxidation state of $Mn^{3.5+}$ and appears as one on the NMR signal.

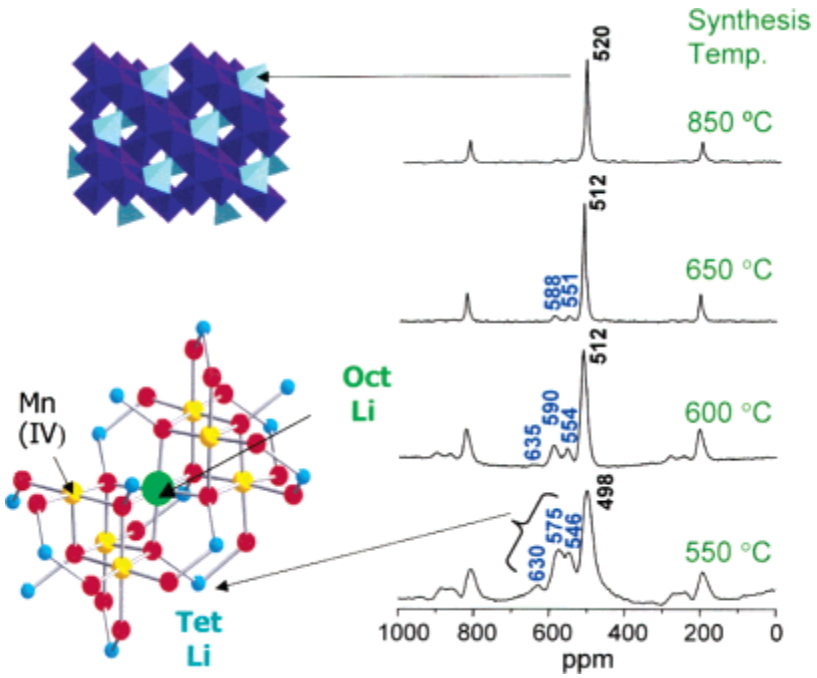


**Figure 2.9** $^{6}$Li MAS NMR spectra of the spinel $LiMn_2O_4$ based on sintering temperature [10].

In the case of $LiCoO_2$ related materials, the NMR spectra show the oxidation of $Co^{3+}$ and doped ions, as well as changes in the electronic conductivity of these materials. This is because the NMR spectra are very sensitive to the semiconductor to transition metal phase transition. Low-spin $Co^{3+}$ ions are normally diamagnetic, but they exhibit very poor paramagnetism for layered $LiCoO_2$ which is temperature-independent. Mainly, the $^{6}Li$ and $^{7}Li$ MAS NMR spectra on $LicoO_2$ are all found at -0.2 ppm, consistent with the presence of essentially spinel localized environments and low-spin $Co^{3+}$ ions.

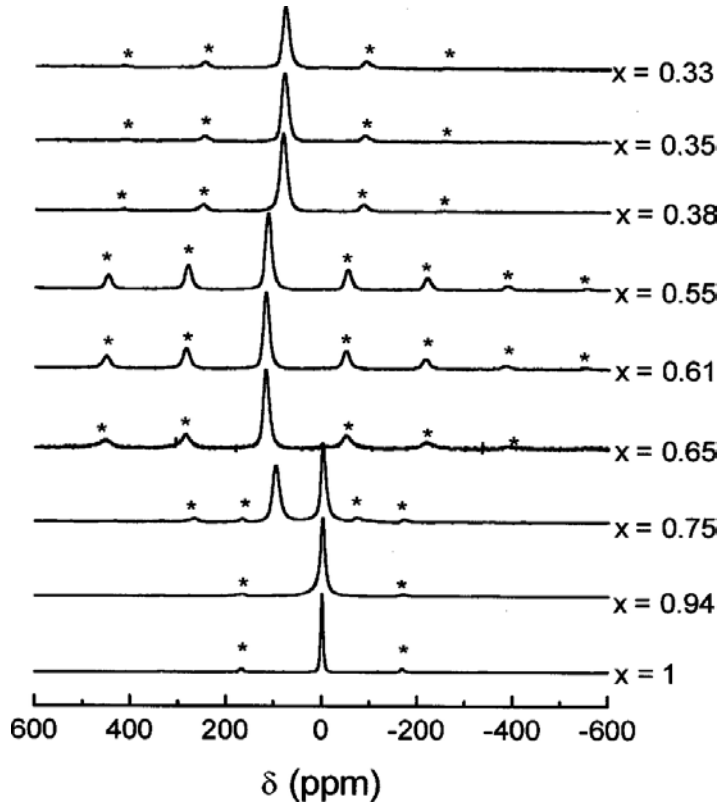


**Figure 2.10** $^{7}$Li MAS NMR spectra of various $Li_xCoO_2$ (0.33< x <1) deintercalated phases recorded with a single-pulse sequence at 13 kHz spinning speed and the spinning sidebands are marked with asterisks (*) [11].

In the case of an olivine structure such as $LiFePO_4$, $LiMnPO_4$, and $LiNiPO_4$, a single resonance with a spinning sideband was observed for all compounds indicating the presence of a localized environment in the lithium cation and a very small range of shift of -90 to 70 ppm relative to the spinel structure appear. This is called the inductive effect of the phosphate group and it is expected that the covalent bond of P-O increases the ionic character of the Li-O and M-O bonds, thereby reducing the overlap and hence the degree of hyperfine interactions in these materials.

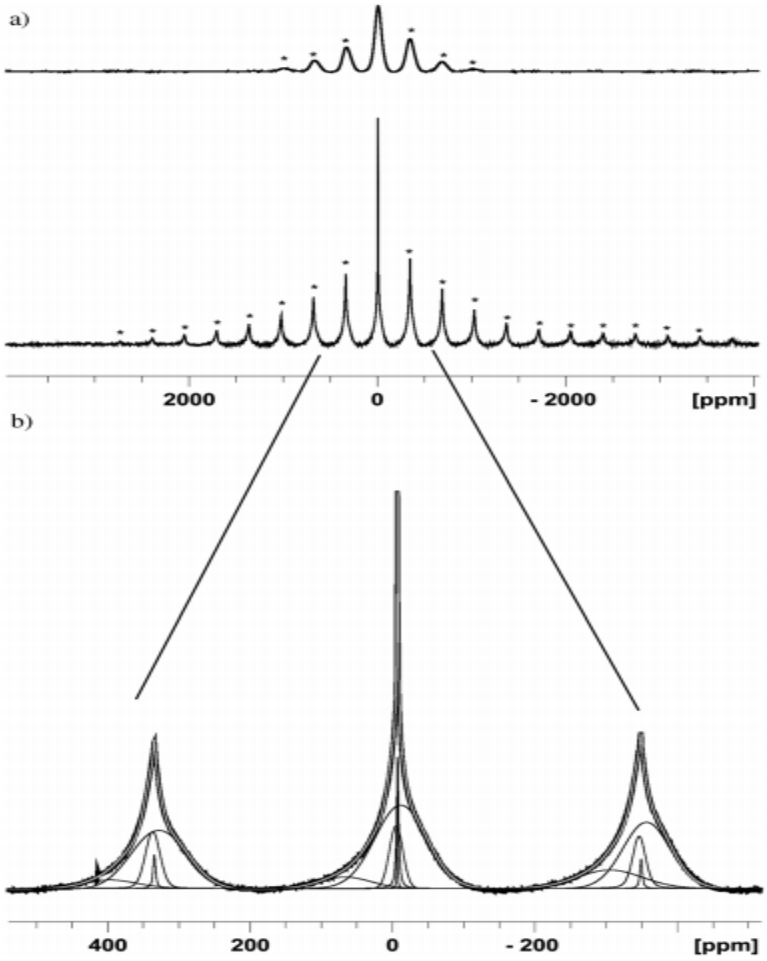


**Figure 2.11** (a) $^{7}$Li MAS NMR spectra of $LiFePO_4$ ($1^{st}$) and biphasic $Li_{0.5}FePO_4$ ($0.5LiFePO_4$:$0.5FePO_4$) ($2^{nd}$). (b) Deconvolution of biphasic $Li_{0.5}FePO_4$ with MAS = 40 kHz and the spinning sidebands are marked with asterisks (*) [12].

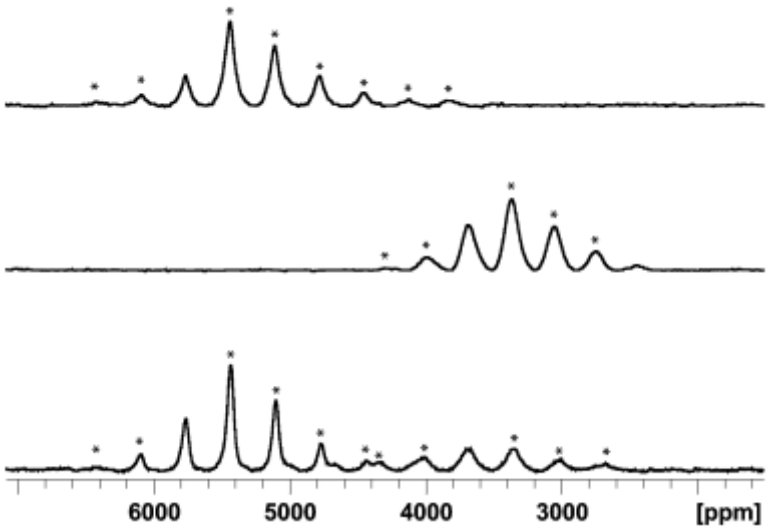


**Figure 2.12** $^{31}$P MAS NMR of $FePO_4$ (top), $LiFePO_4$ (middle) and biphasic $Li_{0.5}FePO_4$ (bottom) all at room temperature. Isotropic shifts for $FePO_4$, $LiFePO_4$ are found at 5800 and 3800 ppm respectively and the spinning sidebands are marked with asterisks (*) [12].

## 3. Experimental

### 3.1 Synthesis

#### 3.1.1 Solid state reaction

Solid-state reaction is the most common method to prepare ceramics, in which solid precursors are ball-milled together, followed by heat-treatment of the resultant mixture in a furnace [36]. In the case of $Li_3V_2(PO_4)_3$, the raw reactants generally involve not only lithium (e.g., LiF, $Li_2CO_3$, LiOH, or $CH_3COOLi$), vanadium (e.g., $V_2O_5$, or $NH_4VO_3$), and phosphorous (e.g., $NH_4H_2PO_4$ or $(NH_4)_2HPO_4$) sources, but also carbon-containing (e.g., acetylene black) or organic compounds (e.g., glucose) [37–40]. In this study, using $H_3BO_3$ as starting material was considered for the introduction of $(BO_3)^{-3}$ unit instead of $(PO_4)^{-3}$ unit. We also tried to obtain high crystalline $Li_3V_2(BO_3)_3$ at low calcination temperature using $V_2O_3$, a low valence stable and less toxic vanadium source. The sample was prepared by solid-state reaction using sucrose as carbon source [41,42]. Stoichiometric amounts of $LiOH{\cdot}H_2O$ (98.0%, Junsei), $V_2O_3$ (95%, Alfa aesar), $H_3BO_3$ (99.5%, Kanto) and sucrose (95.00%, Junsei) (5.6 wt.% in final product) were firstly ball-milled for 1 h in the medium of acetone with a rotation rate of 300 rev/min. The mixture was put into a drying oven at 80 °C for overnight. The precursors are initially heated at 450 °C for 5 h to expel $H_2O$ and $CO_2$ due to organic partly decomposing and then calcined at 700 °C for 12 h

under argon atmosphere.

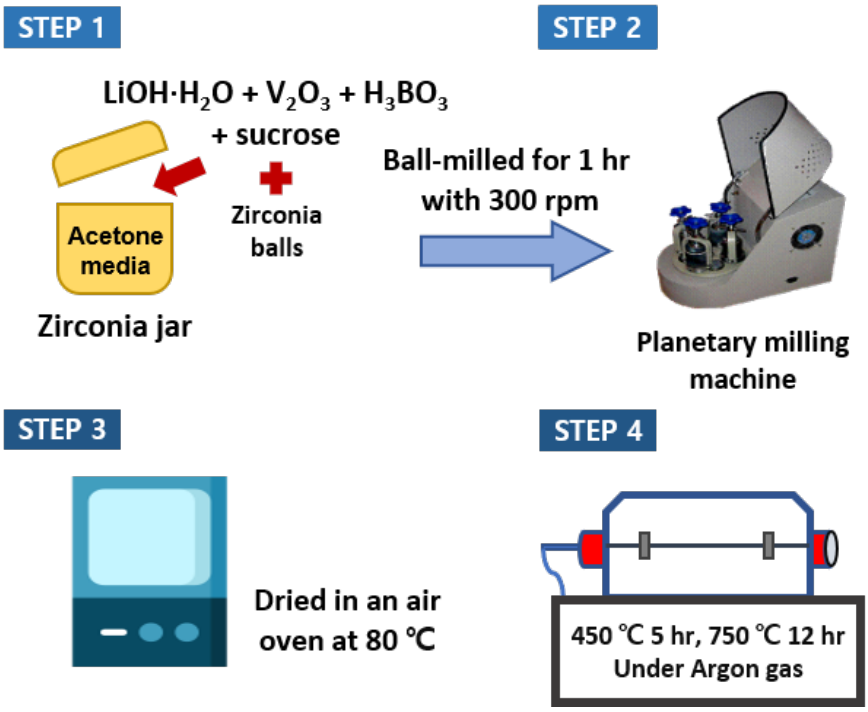


**Figure 3.1** Solid-state synthetic procedures of $Li_3V_2(BO_3)_3$/C as a cathode material.

### 3.1.2 Sol-gel chemistry

Sol-gel synthesis is a wet chemical approach for producing solid materials from small molecules and is considered to be a promising route to design nanosized electrode materials for LIBs [43]. It is because that the sol-gel method has a series of advantages over the traditional solid-state reaction, such as homogeneous mixing the reactants at the atomic or molecular level, low synthesis temperature, short heating time, small particle size on a nanometer scale and uniform particle distribution [44]. The sol-gel process is the conversion of a colloidal suspension (sol) into an integrated 3D network (gel) with pores of sub-micrometer dimensions and polymeric chains whose average length is greater than 1 mm [45].

### 3.1.2.1 Oxalic acid assisted sol-gel method

Pure $Li_3V_2(BO_3)_3$ synthetic conditions were considered to using $Li_2CO_3$, $V_2O_5$, $H_3BO_3$, and oxalic acid as starting materials [46]. Oxalic acid was used here not only as a chelating reagent but also as a reducing agent. First, oxalic acid (99.5%, SCI) and $V_2O_5$ (99.0% Alfa Aesar) in a stoichiometric ratio (3:1) were dissolved in deionized water with magnetic stirring at 90 °C. After a clear green solution formed, a mixture of stoichiometric $Li_2CO_3$ (99.0%, Sigma-Aldrich) and $H_3BO_3$ (99.5%, Kanto) was added to the solution while stirring for 2~3 hr, and then a gel formed and dried in an air oven at 100 °C. The precursor was heated at 350 °C in an argon atmosphere for 6 hr to expel gases (e.g., CO, $CO_2$, $H_2O$), and the obtained product was grounded, and sintered at 700 °C for 4 hr in the argon atmosphere.

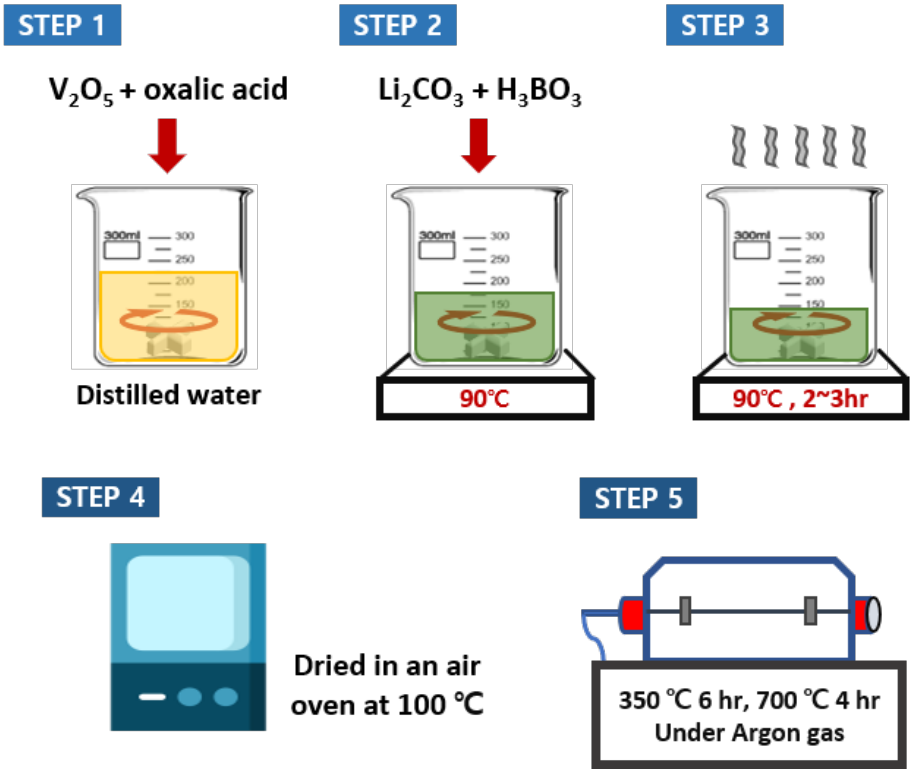


**Figure 3.2** Oxalic acid assisted sol-gel method synthetic procedures of $Li_3V_2(BO_3)_3$ as a cathode material.

### 3.1.2.2 Citric acid assisted sol-gel method

$Li_3V_2(BO_3)_3$/carbon composite material was prepared by a sol–gel route based on citric acid using $NH_4VO_3$ as a vanadium source in this study. First, citric acid (99.5%, Junsei) and $NH_4VO_3$ (99.0%, Alfa Aesar) in a stoichiometric ratio (1:1) were dissolved in deionized water with magnetic stirring at 90 °C. After a clear blue solution formed, a mixture of stoichiometric $LiNO_3$ (98.0%, Junsei) and $H_3BO_3$ (99.5%, Kanto) was added to the solution while stirring for 2~3 hr, and then a gel formed and dried in an air oven at 100 °C. The precursor was heated at 350 °C in an argon atmosphere for 3 hr to expel gases (e.g., $NH_3$, $NO_2$, $H_2O$), and sintered at 400~600 °C for 5 hr in the argon atmosphere. During the synthesis of $Li_3V_2(BO_3)_3$, citric acid as a chelating agent for vanadium facilitated the formation of the homogenous precursor gel; moreover, its decomposition at higher temperatures in an inert atmosphere [47,48] provided the well-dispersed carbon that was used as the selective reduction agent for $V^{5+}$ and the coating material for $Li_3V_2(BO_3)_3$ [49,50].

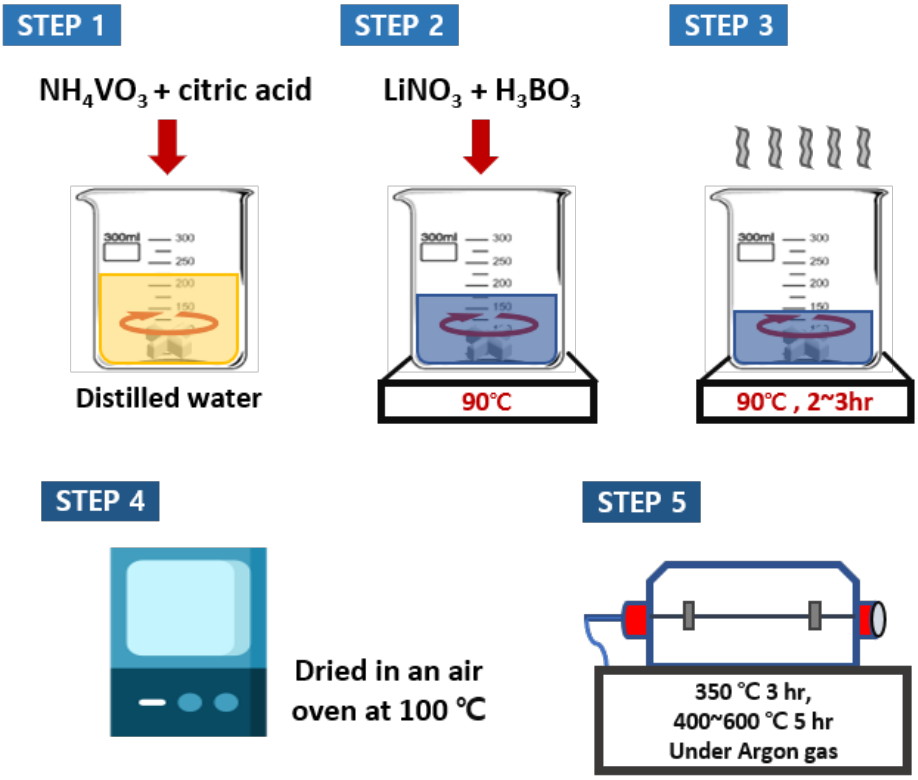


**Figure 3.3** Citric acid assisted sol-gel method synthetic procedures of $Li_3V_2(BO_3)_3$/C as a cathode material.

### 3.2 General characterization of cathode materials

X-ray diffraction (XRD) patterns of the annealed cathode materials were measured by using a Rigaku Ultima 4 diffractometer with Cu $K_\alpha$ radiation ($\lambda$ = 1.5406 Å). The surface morphology and grain sizes of the prepared cathode materials were identified by JEOL JSM-6500F field emission scanning electron microscope (FE-SEM). Transmission electron microscope (TEM) image were acquired by Hitachi H-8100 TEM. XPS analyses of $Li_3V_2(BO_3)_3$ composite was performed using a Thermo Fisher K-Alpha in wide scan survey mode and high-energy resolution. Elemental quantification and chemical state assessment were obtained by full K-alpha evaluation.

### 3.3 Electrochemical test of cathode materials

For the electrochemical characterization, electrodes were fabricated using the synthesized cathode materials. The slurry was prepared by mixing active material, conductive material (super-P) and Polyvinylidene fluoride (PVDF, Aldrich, $M_w$ = 534,000) used as a binder with N-methyl pyrrolidone (NMP) at a weight ratio (wt.%) of 80: 10: 10 for electrode fabrication. and the resulting slurry was pasted on aluminum foil for current collector and dried in a vacuum oven at 80 °C for 2 hr. After that, they were squeezed using a roll press for uniformity of the electrode thickness and then, the electrode with active material was assembled into 2016-coin cells in an argon-filled glove box. Non-aqueous 1.15 M $LiPF_6$ in EC/DMC/DEC (ethylene carbonate/dimethyl carbonate/diethyl carbonate) with a volume ratio of a 3:4:3 was used as the electrolyte. The cell was charged and discharged over a voltage range from 1.0 to 4.5 V versus $Li/Li^+$ electrode and electrochemical cycle tests and cyclic voltammetry (CV) were performed at a scan rate of 0.05mV/s using a galvanostatic automatic battery cycler (WonATech WBCS3000, Korea) at ambient temperature.

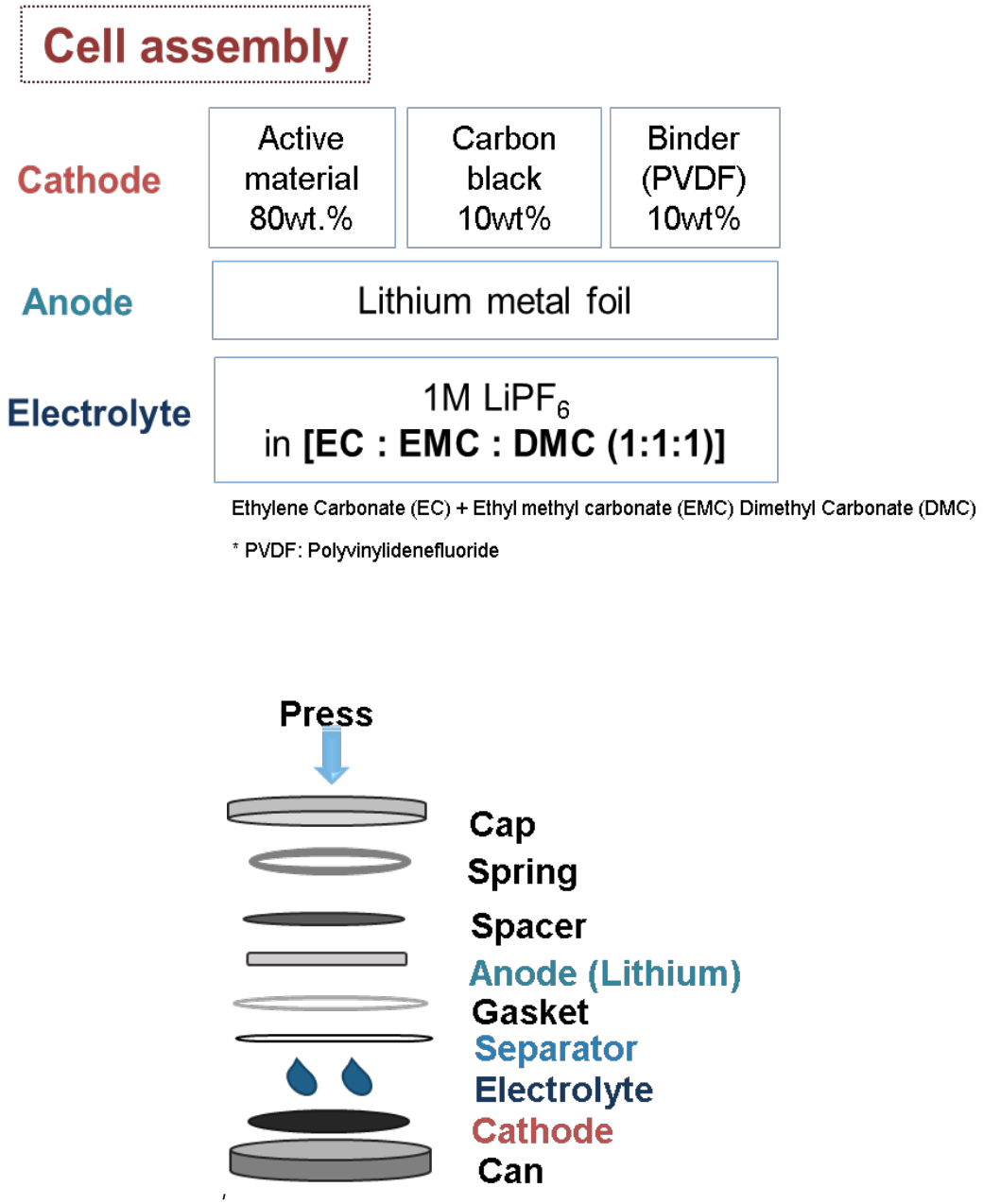


**Figure 3.4** Illustration of synthetic cathode and coin cell assembly of lithium vanadium borate composite as cathode material.

### 3.4 Solid-state MAS NMR study of cathode materials

$^{7}$Li and $^{51}$V MAS NMR were measured by using a Bruker Avance III 300 with a 7.04 T magnet at room temperature. For the MAS NMR experiments, a 2.5 mm MAS probe was used at 116.64 MHz for $^{7}$Li and 78.94 MHz for a $^{51}$V resonance frequency with zirconia rotor. The $^{7}$Li NMR spectrum was referenced to the external 1M LiCl and $^{51}$V NMR spectrum to the powder of $V_2O_5$. The single pulse for $^{7}$Li and $^{51}$V were used to observe the NMR signal and the sample spinning rate was 25 kHz, 20 kHz about each $^{7}$Li and $^{51}$V. The $^{7}$Li spectra were acquired with a 90° pulse length of 1.4 μs, repetition delay of 2 s, 256 transients, and spectral width of 0.23 MHz. For $^{51}$V NMR, the 90° pulse length of 1.5 μs, repetition delay of 1 s, and 1K transients with spectral width of 0.24 MHz were used.


**Figure 3.5** Bruker Avance III 300MHz NMR.

**Figure 3.6** NMR tube and spinner.

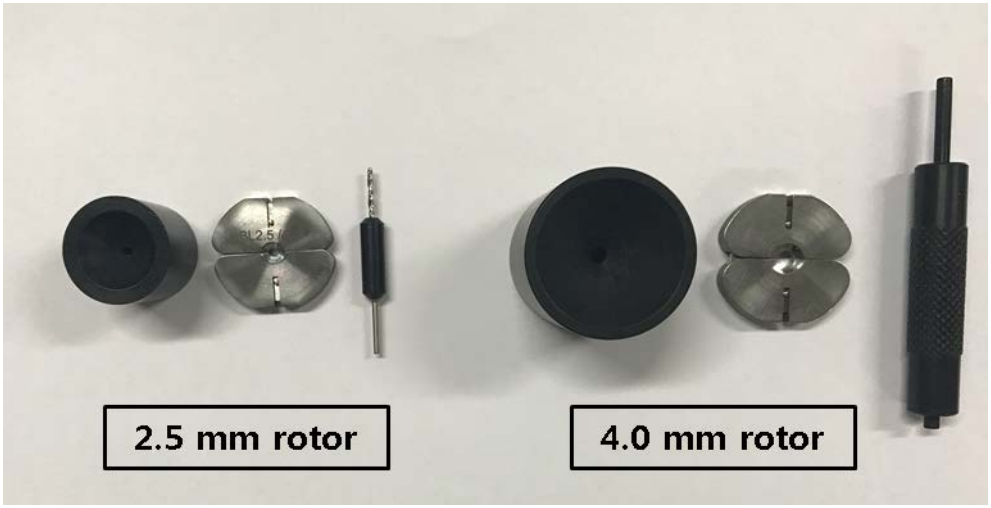


**Figure 3.7** Sampling kit for solid-state NMR.

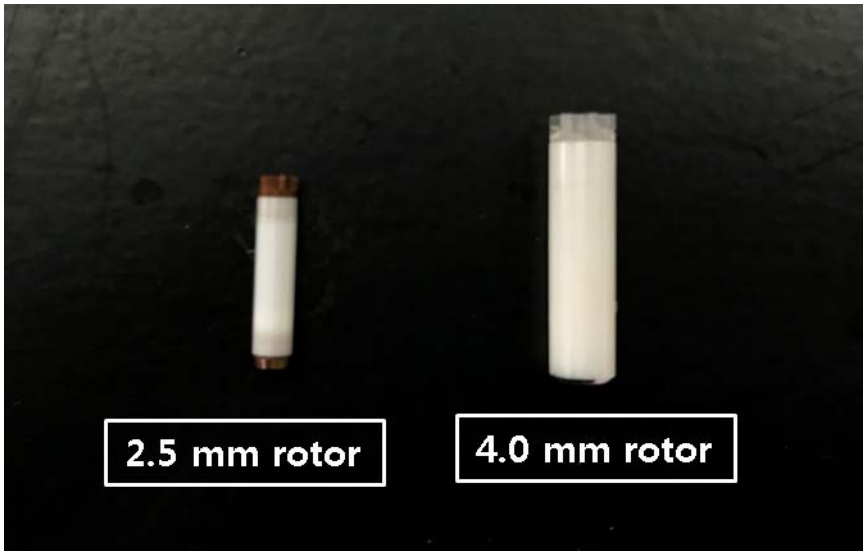


**Figure 3.8** 2.5 mm and 4.0 mm rotor for solid sample container.

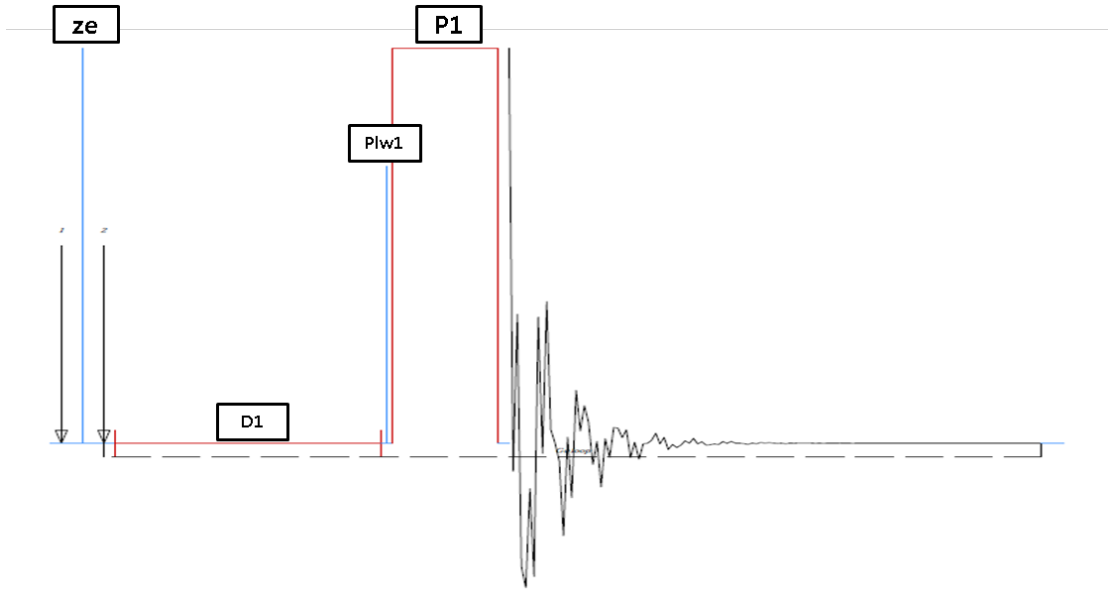


**Figure 3.9** One-pulse (single pulse) parameter.

## 4. Results and Discussion

### 4.1 The effect of preparing method on physical and electrochemical properties of cathode materials

#### 4.1.1 X-ray Diffraction (XRD) for structural characterization

XRD is useful for determining the crystal structure of a solid sample by measuring the diffraction according to the angle change of the X-ray irradiating the sample. As a result of the experiments, all X-ray diffraction patterns of each cathode materials are shown different patterns. Figure 4.1, 4.2 and 4.3 show the XRD patterns of $Li_3V_2(BO_3)_3$/C prepared by the solid-state method, oxalic acid assisted sol-gel method and citric acid assisted sol-gel method respectively. The observed XRD patterns indicate that $Li_3V_2(BO_3)_3$ cathode materials are mixed phase of several components.

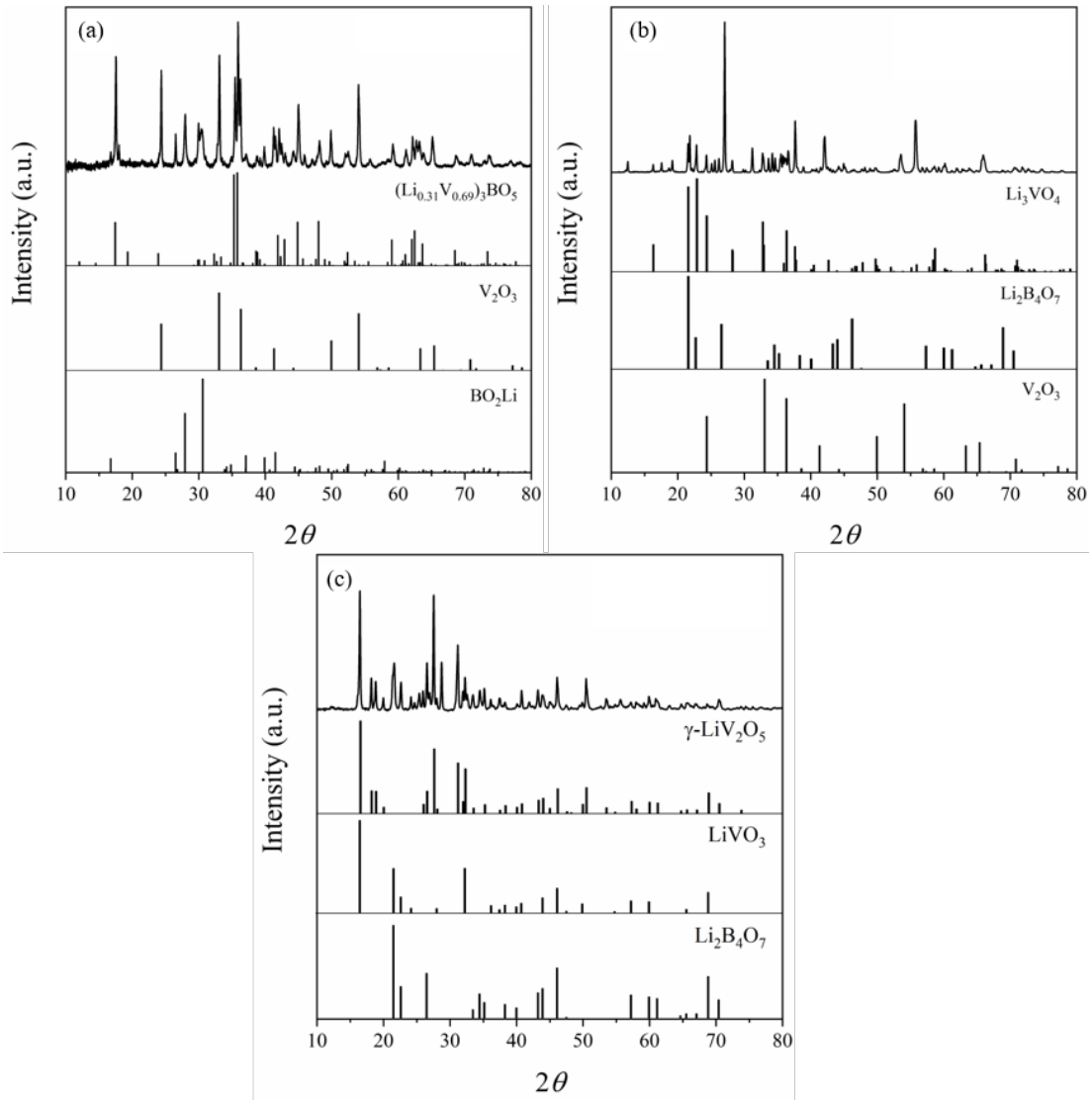


**Figure 4.1** The XRD patterns of $Li_3V_2(BO_3)_3$/C prepared by (a) solid-state method, (b) oxalic acid assisted sol-gel method and (c) citric acid assisted sol-gel method

### 4.1.2 Energy dispersive spectroscopic (EDS) characterization

The combination of scanning electron microscopy (SEM) imaging of the specimen microstructure and analysis of local elemental composition via energy dispersive X-ray spectrometry (EDS) is the most powerful and robust elemental characterization technique that widely applied in science, engineering [51]. SEM images and the corresponding EDS elemental mapping of the lithium vanadium borate composite samples prepared by the solid-state method, oxalic acid assisted sol-gel method and citric acid assisted sol-gel method are shown in Figure 4.4, 4.5 and 4.6 respectively. Homogeneous distribution of V, O and B elements was observed at each particle, it implies that successful synthesis of the lithium vanadium borate composite with a porous morphology.

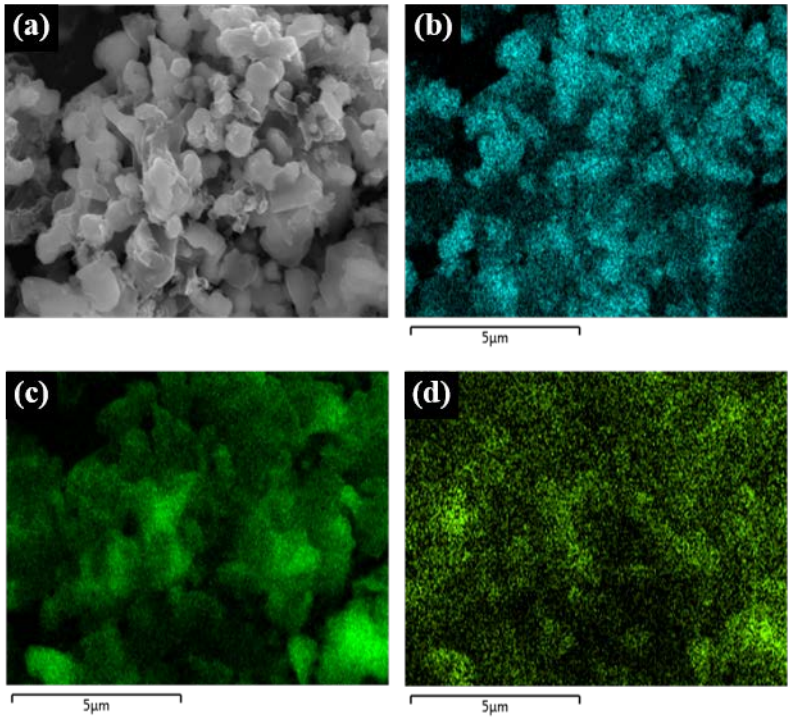


**Figure 4.2** SEM image and the corresponding EDS elemental mapping of the $Li_3V_2(BO_3)_3$/C prepared by solid-state method (a) SEM image, (b) V, (c) O and (d) B elements.

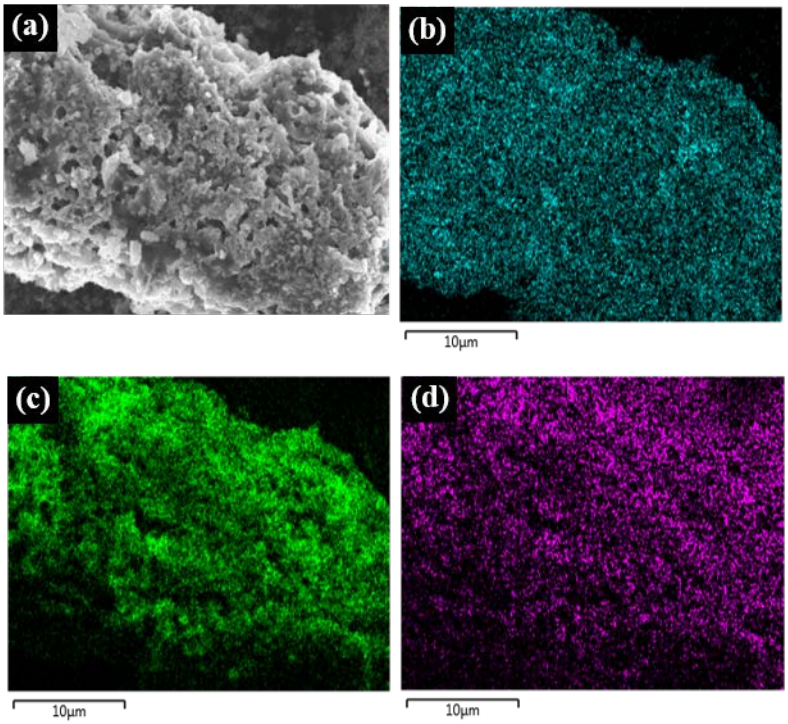


**Figure 4.3** SEM image and the corresponding EDS elemental mapping of the $Li_3V_2(BO_3)_3$ prepared by oxalic acid assisted sol-gel method (a) SEM image, (b) V, (c) O and (d) B elements.

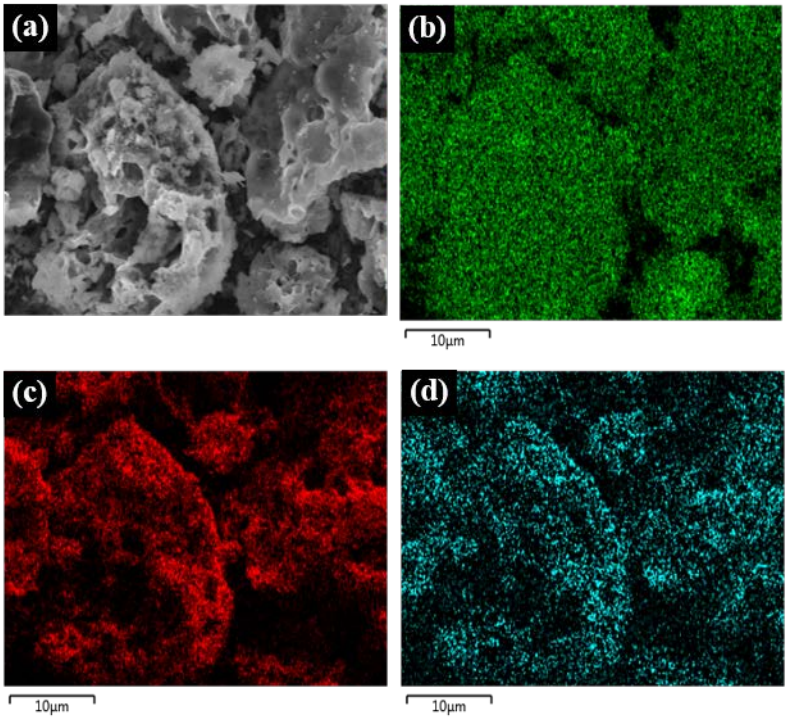


**Figure 4.4** SEM image and the corresponding EDS elemental mapping of the $Li_3V_2(BO_3)_3$/C prepared by citric acid assisted sol-gel method (a) SEM image, (b) V, (c) O and (d) B elements.

### 4.1.3 Electrochemical properties

The electrochemical performance of each cathode material according to the synthesis method was observed. Figure 4.7 shows that the initial charge and discharge curves measured at 0.05C for each material synthesized by different methods. Among the initial discharge capacities, $Li_3V_2(BO_3)_3$/C prepared via citric acid assisted sol-gel method was the highest discharge capacity (195 mAh $g^{-1}$). $Li_3V_2(BO_3)_3$ prepared with the solid-state method and oxalic acid assisted sol-gel method were 41 mAh $g^{-1}$, and 27 mAh $g^{-1}$ respectively. Also, $Li_3V_2(BO_3)_3$/C prepared via citric acid assisted sol-gel method can observe three voltage plateaus at 0.9-4.5V. Figure 4.8 (Ⅰ) and (Ⅱ) shown electrochemical performance of synthesized cathode material at different current rate (C-rate) and long cyclabilities (50 cycle) at 1.0 C. The results show that $Li_3V_2(BO_3)_3$/C prepared with citric acid assisted sol-gel method has outstanding performance in all current ranges.

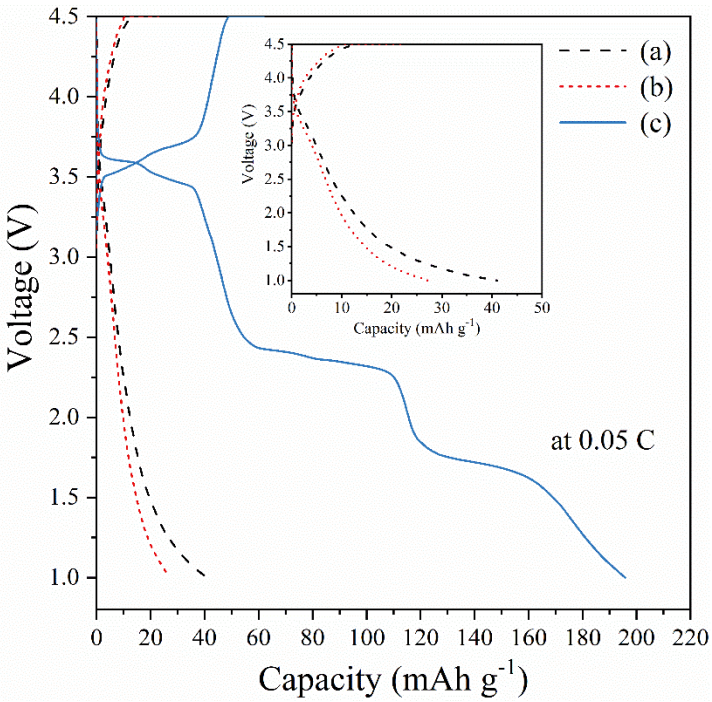


**Figure 4.5** Initial charge-discharge curves of $Li_3V_2(BO_3)_3$ composite prepared with (a) solid-state method, (b) oxalic acid assisted sol-gel method, and (C) citric acid assisted sol-gel method.

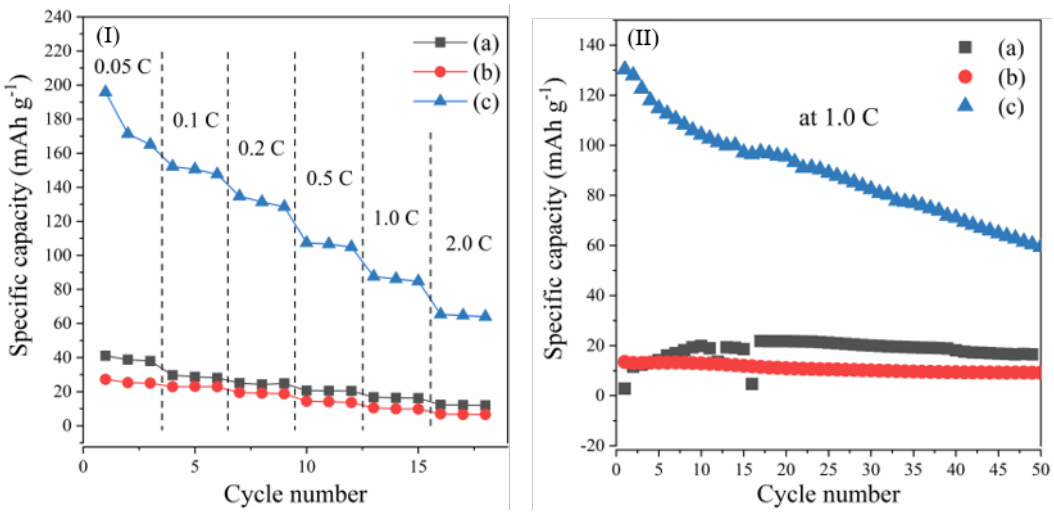


**Figure 4.6** (Ⅰ) Rate performance at various C-rate and (Ⅱ) long cyclabilities of $Li_3V_2(BO_3)_3$ composite prepared with (a) solid-state method, (b) oxalic acid assisted sol-gel method, and (C) citric acid assisted sol-gel method.

## 4.2 Optimization of citric acid assisted sol-gel synthesis routine

### 4.2.1 Thermal analysis: Thermogravimetric Analysis (TGA) and Differential Scanning Calorimetry (DSC)

Thermal analysis was performed by thermogravimetric analysis (TGA) and differential scanning calorimetry (DSC) (TGA–DSC, SDT Q600, TA Instruments, USA) at a heating rate of 10 ℃ $min^{-1}$. The TG curve of the precursor, Figure 4.7, shows three obvious weight loss steps between 152.3 ℃ and 235.0 ℃. The first one over 150 ℃ is related to the dehydration of the hydrates. The second one at about 235 ℃ is associated with thermal decomposition of starting materials. The corresponding DSC curve shows two exothermic peaks at 205.2 ℃ and 595.5 ℃ that is related to the formation of $Li_3V_2(BO_3)_3$ compound. Also, we can observe single plateau of heat flow from 315.9 to 579.1 ℃. This is confirmed by successive thermal treatments at temperatures ranging from 300 to 600 ℃. The TGA / DSC patterns indicate that the pyrolysis of starting materials and the formation of $Li_3V_2(BO_3)_3$ are in the same temperature range, which makes it possible to coat carbon in situ during the synthesis of $Li_3V_2(BO_3)_3$.

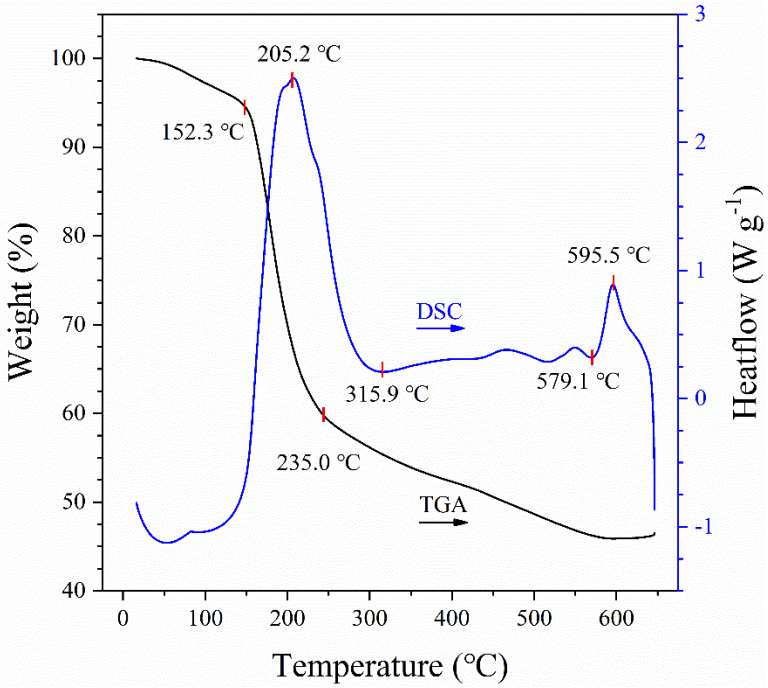


**Figure 4.7** DSC/TGA curves of precursor containing $LiNO_3$, $NH_4VO_3$, $H_3BO_3$, and citric acid

### 4.2.2 X-ray Diffraction (XRD) for structural characterization

This material is measured at different sintering temperatures of 400 ℃, 450 ℃, 500 ℃, 550 ℃ and 600 ℃, respectively. Figure 4.8 shows the XRD patterns of sintered at various temperature. And results are shows that no significant change in XRD patterns of materials sintered from 450 to 550 ℃. The observed XRD profile clearly indicates the formation of the mixed phase of orthorhombic $LiV_2O_5$ phase (01-074-0055) (space group P21/m) [52] with the minor phase of monoclinic $LiVO_3$ already discussed at chapter 4.1.1. (JCPDS Card no.: (00-039-0378), space group: C2/c) [53]

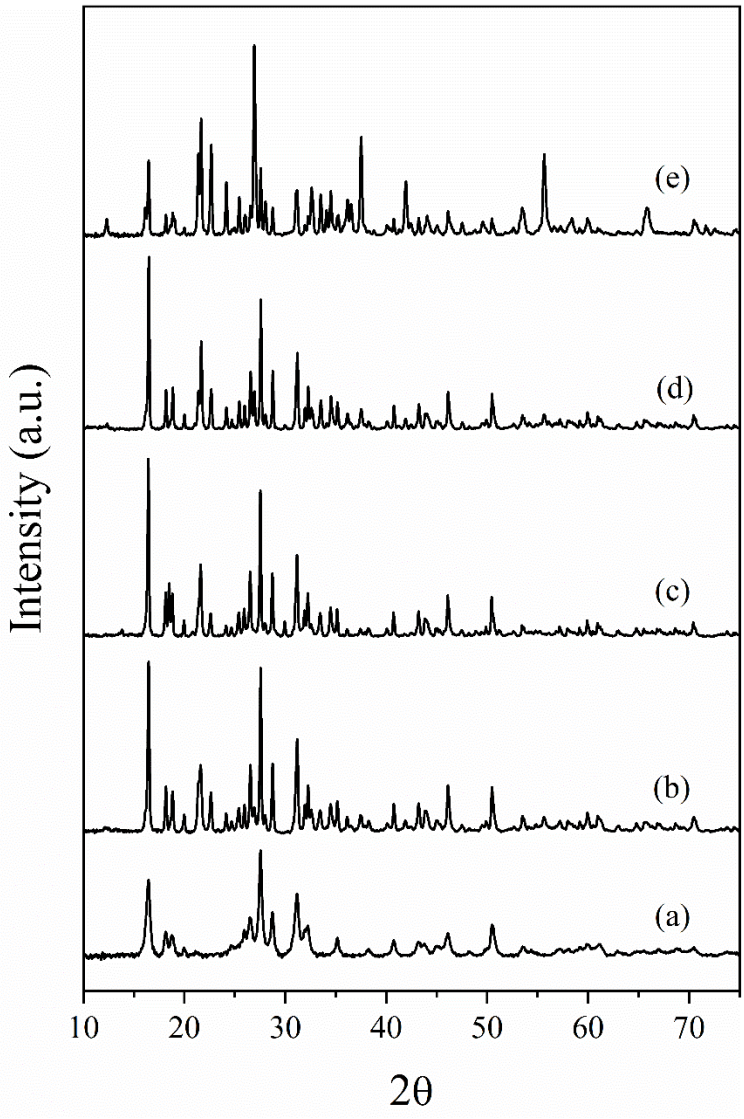


**Figure 4.8** The XRD patterns of $Li_3V_2(BO_3)_3$/C sintered at various temperature.

(a) 400 ℃, (b) 450 ℃, (c) 500 ℃, (d) 550 ℃ and (e) 600 ℃

### 4.2.3 Scanning Electron Microscopy (FE-SEM) and Transmission Electron Microscopy (HR-TEM) analysis for morphological study

Figure 4.9 show five SEM images to analyze the morphology of $Li_3V_2(BO_3)_3$/C sintered at various temperature (from 400 to 600 ℃). The materials which sintered from 400 to 500 ℃ are showed the rough and highly porous of the grains. On the other hand, we can observe fine crystal grains are formed at 550 ℃, and it is grown-up in size of crystal grains at 600 ℃. And all materials are mainly composed of micro sized grains and large pores with diameter in the range of 0.5 -1 μm. The novel microporous morphology is more suitable and effective for electrolyte to permeate into the inside of the electrode which is profitable to the high performance of the $Li_3V_2(BO_3)_3$/C [54].

Also, to determine the lattice and morphology of the particles, the particle shape was measured using HR-TEM.

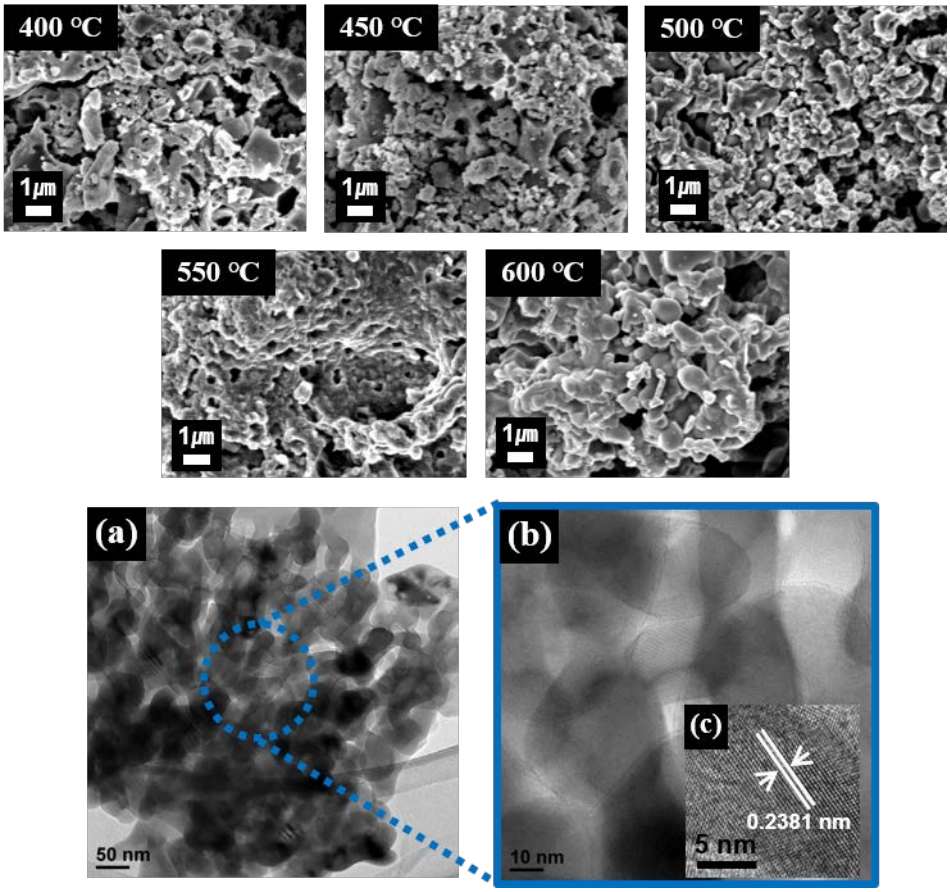


**Figure 4.9** SEM images of $Li_3V_2(BO_3)_3$/C sintered at various temperature (from 400 to 600 ℃). Also, TEM images (a), (b) and (c) HR-TEM image of $Li_3V_2(BO_3)_3$/C sintered at 450 ℃

## 4.3 Characterization of electrochemical and physical properties of $Li_3V_2(BO_3)_3$

### 4.3.1 X-ray photoelectron spectroscopy (XPS) analysis for oxidation state of cathode material

XPS analyses were carried out to investigate the chemical composition and oxidation state of the metal ions Li, V, B, O and C in $Li_3V_2(BO_3)_3$/C. Figure 4.10 (a) presents the XPS survey spectra of $Li_3V_2(BO_3)_3$/C which clearly reveals the peaks of Li, V, B, O and C. Figure 4.10 (b) display the XPS spectra of Li1s appears as a single peak with the binding energy (BE) 55.6 eV. The BE values of Li1s is consistent with +1 oxidation state of Li in $Li_3V_2(PO_4)_3$ as reported earlier [55] and +3 oxidation state of B in pure $B_2O_3$ [56]. Figure 4.10 (d) shows that fitting of the V2p core level spectra using a Gaussian Lorentzian fit in to two peaks at 517.3 eV and 524.6 eV, which is assigned to the $V2p_{1/2}$ and $V2p_{3/2}$. It was found that the binding energy for the $V2p_{1/2}$ and $V2p_{3/2}$ peaks are well matched with the BE values those measured in $LiVOPO_4$ for the $V^{4+}$ [57]. Figure 4.10 (e) showed the C1s peak with a binding energy of 283.8 eV exist in the spectra which suggests that the citrate was decomposed into carbon during calcination, and residual carbon exists in $Li_3V_2(BO_3)_3$/C [55] while the C1s peak at 289 eV for C—O is absent used for the calibration of instrument. This is profitable to increase the electronic conductivity for $Li_3V_2(BO_3)_3$/C. The O1s peak located at 529 and 531.3 eV as shown in figure 4.10 (f). It has been confirmed[58–60] that the difference in binding energies between the O1s ($VO_x$)

core level, normally taken at 530.0 eV, and the $V2p_{3/2}$ level

$$\Delta = BE(O1s) - BE\ (V2p_{3/2}) \quad \text{(Equation 4.1)}$$

is better for use in the determination of the oxidation state of the vanadium.

Figure 4.10 (d) shows to two main peaks at 523.7 eV and 516.3 eV which is assigned to the $V2p_{1/2}$ and $V2p_{3/2}$. The change of the V2p core level peak results from the decrease of the higher binding energy peak at $EB(V2p_{3/2A})$ = 516.3 eV and the increase of the lower binding energy peak at $EB(V2p_{3/2B})$ = 514.9 eV. It is due to the partial reduction of vanadium $V^{5+}$ into $V^{4+}$ ions. Only two vanadium oxidation states (5+ and 4+) were observed after substitution on our samples prepared by thermal oxidation of vanadium metal [61]. Hence it can be concluded that the oxidation state of Li, and V in $Li_3V_2(BO_3)_3$/C are +1, +4.5, respectively.

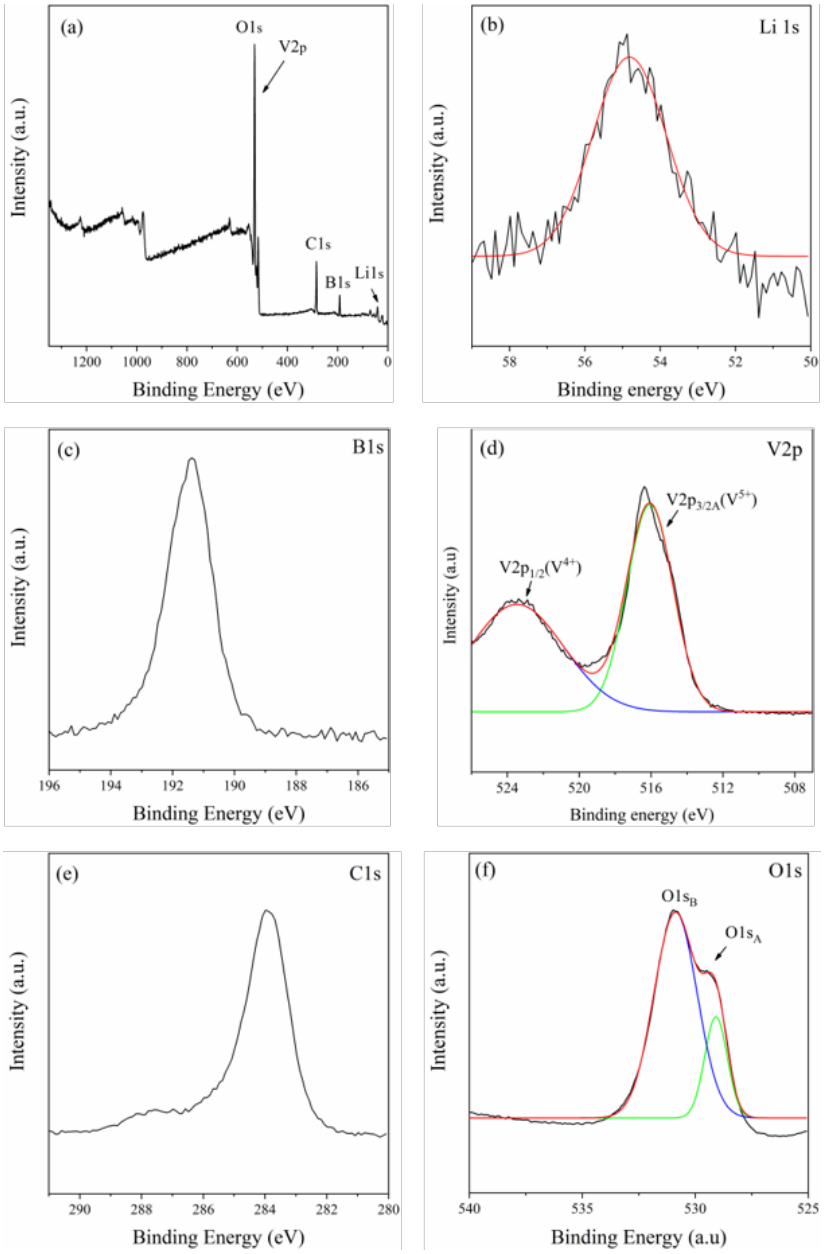


**Figure 4.10** The XPS spectra of $Li_3V_2(BO_3)_3$/C. (a) Survey spectrum, (b) Lithium, (c) Boron, (d) Vanadium, (e) Carbon and (f) Oxygen.

### 4.3.2 Electrochemical properties

#### 4.3.2.1 Rate performances, long cycle abilities

The electrochemical performances of the $Li_3V_2(BO_3)_3$/C sintered from 400 to 600 ℃ are shown in Figure 4.11. In Figure 4.11 (Ⅰ), the initial discharge capacities of $Li_3V_2(BO_3)_3$/C sintered at various temperature (a) 400 ℃, (b) 450 ℃, (c) 500 ℃, (d) 550 ℃ and (e) 600 ℃ at 0.05 C-rate were measured 206.5, 195.8, 220.7, 140.7, and 57.2 mAh $g^{-1}$ respectively. The $Li_3V_2(BO_3)_3$/C sintered at 500 ℃ was shown highest initial discharge capacities, but as C-rate is higher, LVB synthesized at 450 ℃ has shown superior performance.

Long cycle ability test was performed at 1.0 C in Figure 4.11 (Ⅱ), the material synthesized at 450 ℃ shows the outstanding overall performance. Also, the capacity retention rate was 57%.

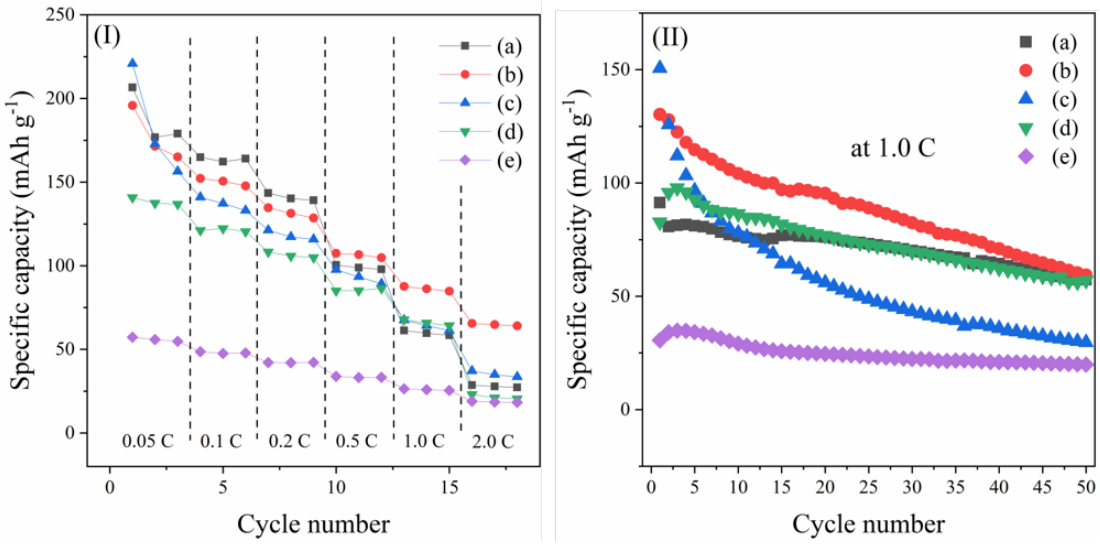


**Figure 4.11** (Ⅰ) Rate performance and (Ⅱ) cycling cyclabilities of $Li_3V_2(BO_3)_3$/C sintered at various temperature. (a) 400 ℃, (b) 450 ℃, (c) 500 ℃, (d) 550 ℃ and (e) 600 ℃

#### 4.3.2.2 Electrochemical behavior of $Li_3V_2(BO_3)_3$/C

Initial discharge curve of $Li_3V_2(BO_3)_3$/C shows three discontinuous plateau and showed the dissimilar behavior from the phosphate materials (LiMPO4, M=Fe, Mn, Co) where they showed a single continuous discharge plateau due to the single lithium ion site at crystal structure. The observed discontinuous three plateau indicates that different removable lithium ions sites at least two or three. But from the second cycle, three discontinuous plateaus disappeared at charge and discharge curves.

The Cyclic voltammetry (CV) results were obtained to gain understanding the electrochemical behavior about the charge/discharge profiles of LVB/C at the scan rate of 0.05 mV s-1. The five times repeated CV scan results are presented in Figure 4.12. (b). CV curves also shown the unusual change of potential area was observed between the 1st and 2-5th cycles. Two oxidation peaks (3.5 and 3.7 V) and four reduction peaks (3.5, 3.45, 2.3 and 1.6 V) are appeared at first cycle, and two oxidation peaks (2.6 and 3.9 V) and two reduction peaks (3.5 and 2.5 V) are clearly seen since the second cycle.

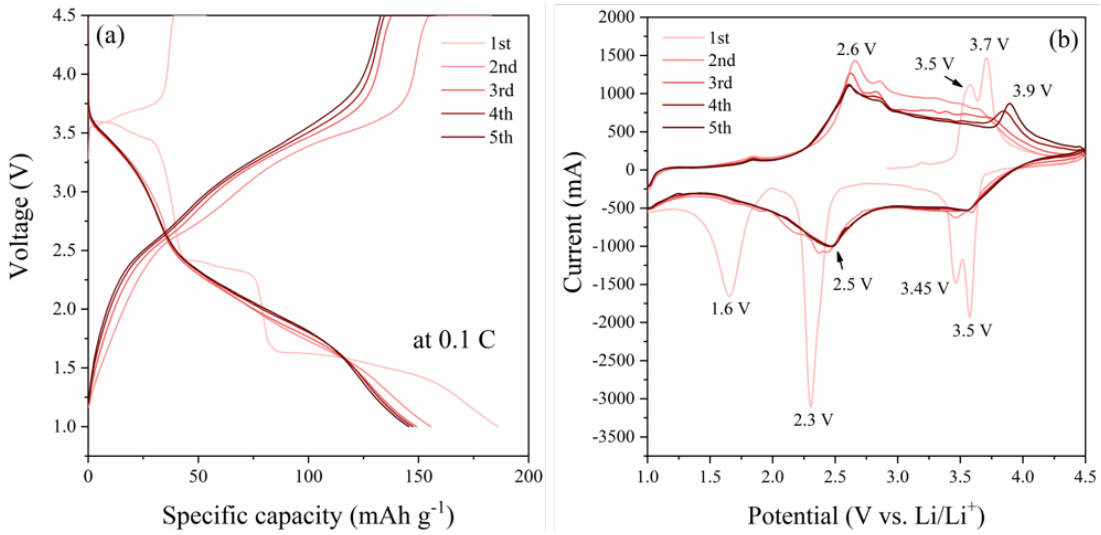


**Figure 4.12** (a) charge and discharge curves and (b) cyclic voltammetry curves of $Li_3V_2(BO_3)_3$/C

### 4.3.3 MAS NMR for structural characterization

#### 4.3.3.1 $^{7}$Li, $^{51}$V MAS NMR

Figure 4.13 shows the information obtained by the solid-state nuclear magnetic resonance (NMR) spectroscopy regarding local environment about lithium and vanadium on structural framework of $Li_3V_2(BO_3)_3$/C. The $^{7}$Li and $^{51}$V MAS NMR spectra are displayed in Figure 4.13 (a) and (b). The $^{7}$Li MAS NMR (Figure 4.13 (a)) shows the existence of a single resonance peak around 0.0 ppm pointed out by arrow and spinning side bands are recognized by asterisks (*) corresponding to the lithium site in LVB/C. The $^{51}$V MAS NMR spectrum displayed in the Figure 4.13 (b) exhibits a broad isotropic resonance at approximately -543.96 ppm with a series of sidebands that span over more than 1500 ppm. We observed only single resonance peak at $^{7}$Li and $^{51}$V spectra, however, these results don't imply that these elements exist as a single site on their crystal structure. It has to be considered as the superimposition of signals coming from a distribution of several lithium ion sites. [62]

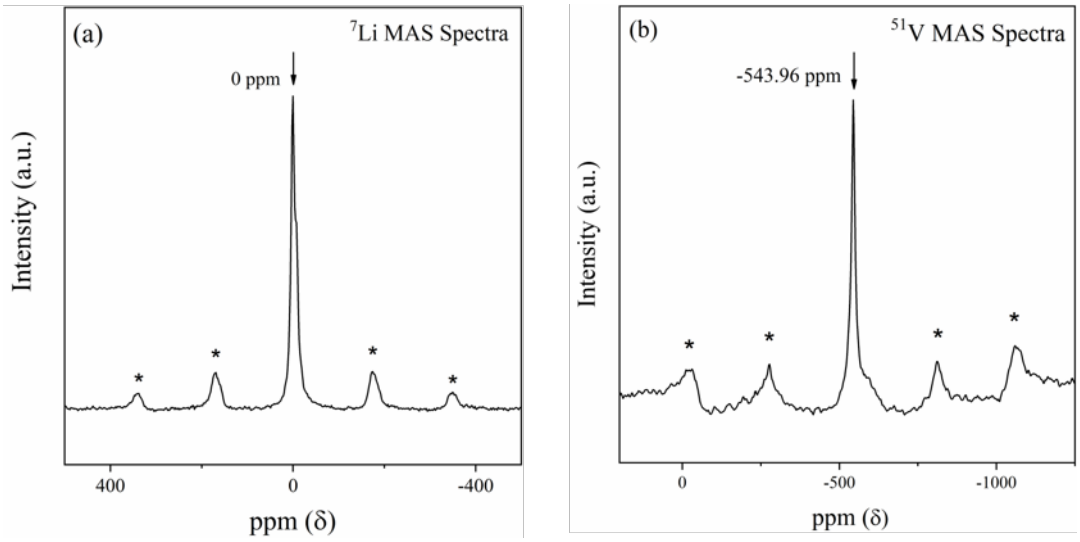


**Figure 4.13** (I) $^{7}$Li and (II) $^{51}$V MAS NMR spectrum $Li_3V_2(BO_3)_3$/C at 25kHz. Isotropic peak is marked as arrow and the spinning sidebands are marked with asterisks (*).

## 5. Conclusions

The preparation of $Li_3V_2(BO_3)_3$/C cathode material for lithium-ion batteries were carried out by the solid-state method, oxalic acid, and citric acid sol-gel method considering various requisite. And for considering effects of preparation methods on cathode materials, wide investigation including structural, surface properties and electrochemical characteristics was performed. Among them, the material synthesized via citric acid assisted sol-gel method showed outstanding performance. Therefore, thermal analysis of the precursor was performed and synthesized from 400 to 600 ℃ for optimizing sintering temperature. The XRD results reveal that same crystal structure when calcination temperature was 450 to 550 ℃. SEM and TEM images were used to confirm the porous morphology and fine crystal grains are formed since 550 ℃. The presence and oxidation state of each element was determined through XPS. Solid-state NMR was measured by $^{7}Li$ and $^{51}V$ MAS NMR spectroscopy. The single isotropic peak and spinning sideband were confirmed by MAS method. The material synthesized at 450 ℃ shows the superior overall electrochemical performance. Cyclic voltammetry (CV) and charge-discharge profile are confirmed that the material has irreversible phase transition. At first discharging step, lithium intercalation on LVB/C as cathode materials were entails some structural modifications. Unknown irreversible structural modifications are observed after first cycle. Moreover, there are no pronounced changes occurs in the shape and

peak intensity for the subsequent cycles, indicating that the $Li_3V_2(BO_3)_3$/C has good cycling stability and reversibility.

## 6. Reference


[1] Aaron Kenneth Schwarz, Lithium Ion Fires & Explosions are Preventable, (2017) 1–6.

[2] J.B. Goodenough, Y. Kim, Challenges for rechargeable Li batteries, Chem. Mater. 22 (2009) 587–603.

[3] C.M. Julien, A. Mauger, K. Zaghib, H. Groult, Comparative issues of cathode materials for Li-ion batteries, Inorganics. 2 (2014) 132–154.

[4] S. Yu, A. Mertens, H. Kungl, R. Schierholz, H. Tempel, R.-A. Eichel, Morphology Dependency of $Li_3V_2(PO_4)_3$/C Cathode Material Regarding to Rate Capability and Cycle Life in Lithium-ion Batteries, Electrochim. Acta. 232 (2017) 310–322.

[5] R. Schurko, Introduction to Solid State NMR, (2002) 1–30. doi:10.1016/j.soilbio.2007.07.004.

[6] N.H.M.F. Laboratory, Magic Angle Spinning Probe, Nationalmaglab. (2014)

[7] S. Matsuoka, M. Inoue, Application of REDOR NMR in natural product chemistry, Chem. Commun. (2009) 5664–5675.

[8] J.D. Biglands, A. Radjenovic, J.P. Ridgway, Cardiovascular magnetic resonance physics for clinicians: Part II, J. Cardiovasc. Magn. Reson. 14 (2012) 66.

[9] A. Felix, E. Rosa, What is the spin echo used for in NMR?, (2012) 36–50.

[10] C.P. Grey, N. Dupré, NMR studies of cathode materials for lithium-ion rechargeable batteries, Chem. Rev. 104 (2004) 4493–4512.

[11] D. Carlier, I. Saadoune, M. Ménétrier, C. Delmas, Lithium Electrochemical Deintercalation from $O_2$ $LiCoO_2$ Structure and Physical Properties, J. Electrochem. Soc. 149 (2002) A1310–A1320.

[12] L.J.M. Davis, I. Heinmaa, B.L. Ellis, L.F. Nazar, G.R. Goward, Influence of particle size on solid solution formation and phase interfaces in $Li_{0.5}FePO_4$ revealed by $^{31}P$ and $^{7}Li$ solid state NMR spectroscopy, Phys. Chem. Chem. Phys. 13 (2011) 5171–5177.

[13] Y. Wang, G. Cao, Developments in nanostructured cathode materials for high-performance lithium-ion batteries, Adv. Mater. 20 (2008) 2251–2269.

[14] J.W. Fergus, Recent developments in cathode materials for lithium ion batteries, J. Power Sources. 195 (2010) 939–954.

[15] R. Koksbang, J. Barker, H. Shi, M.Y. Saidi, Cathode materials for lithium rocking chair batteries, Solid State Ionics. 84 (1996) 1–21.

[16] M.M. Thackeray, C. Wolverton, E.D. Isaacs, Electrical energy storage for transportation—approaching the limits of, and going beyond, lithium-ion batteries, Energy Environ. Sci. 5 (2012) 7854–7863.

[17] M. Armand, J.-M. Tarascon, Building better batteries, Nature. 451 (2008) 652.

[18] M.J. Armstrong, C. O'Dwyer, W.J. Macklin, J.D. Holmes, Evaluating the performance of nanostructured materials as lithium-ion battery electrodes, Nano Res. 7 (2014) 1–62.

[19] G.G. Amatucci, J.M. Tarascon, L.C. Klein, Cobalt dissolution in $LiCoO_2$-based non-aqueous rechargeable batteries, Solid State Ionics. 83 (1996) 167–173.

[20] G.G. Amatucci, J.M. Tarascon, L.C. Klein, CoO2, the end member of the $Li_xCoO_2$ solid solution, J. Electrochem. Soc. 143 (1996) 1114–1123.

[21] B. Deng, H. Nakamura, M. Yoshio, Capacity fading with oxygen loss for manganese spinels upon cycling at elevated temperatures, J. Power Sources. 180 (2008) 864–868.

[22] S. Lee, S.S. Park, Atomistic simulation study of monoclinic $Li_3V_2(PO_4)_3$ as a cathode material for lithium ion battery: structure, defect chemistry, lithium

ion transport pathway, and dynamics, J. Phys. Chem. C. 116 (2012) 25190–25197.

[23] J. Gaubicher, C. Wurm, G. Goward, C. Masquelier, L. Nazar, Rhombohedral form of $Li_3V_2(PO_4)_3$ as a cathode in Li-ion batteries, Chem. Mater. 12 (2000) 3240–3242. doi:10.1021/cm000345g.

[24] S.C. Yin, H. Grondey, P. Strobel, M. Anne, L.F. Nazar, Electrochemical property: Structure relationships in monoclinic $Li_{3-y}V_2(PO_4)_3$, J. Am. Chem. Soc. 125 (2003) 10402–10411. doi:10.1021/ja034565h.

[25] C. Deng, S. Zhang, S.Y. Yang, Y. Gao, B. Wu, L. Ma, B.L. Fu, Q. Wu, F.L. Liu, Effects of Ti and Mg codoping on the electrochemical performance of $Li_3V_2(PO_4)_3$ cathode material for lithium ion batteries, J. Phys. Chem. C. 115 (2011) 15048–15056.

[26] Z. Gong, Y. Yang, Recent advances in the research of polyanion-type cathode materials for Li-ion batteries, Energy Environ. Sci. 4 (2011) 3223–3242.

[27] G. Hautier, A. Jain, H. Chen, C. Moore, S.P. Ong, G. Ceder, Novel mixed polyanions lithium-ion battery cathode materials predicted by high-throughput ab initio computations, J. Mater. Chem. 21 (2011) 17147–17153.

[28] A. Yamada, N. Iwane, Y. Harada, S. Nishimura, Y. Koyama, I. Tanaka, Lithium Iron Borates as High-Capacity Battery Electrodes, Adv. Mater. 22 (2010) 3583–3587.

[29] S. Afyon, D. Kundu, A.J. Darbandi, H. Hahn, F. Krumeich, R. Nesper, A low dimensional composite of hexagonal lithium manganese borate ($LiMnBO_3$), a cathode material for Li-ion batteries, J. Mater. Chem. A. 2 (2014) 18946–18951.

[30] R.H. and Y. Ozery, What is NMR?, Hebr. Univ. (2013).

[31] UNIVERSITY OF NEBRASKA–LINCOLN, Courses: CHEM 991A / INTRO TO

NMR, (2014).

[32] D.A. Skoog, F.J. Holler, S.R. Crouch, Principles of instrumental analysis, Cengage learning, 2017.

[33] J.C. Edwards, Principles of NMR, Process NMR Assoc. LLC, 87A Sand Pit Rd, Danbury CT. 6810 (2009).

[34] F. Taulelle, Fundamental principles of NMR crystallography, NMR Crystallogr. (2009) 245–262.

[35] M.H. Levitt, R. Freeman, NMR population inversion using a composite pulse, J. Magn. Reson. 33 (1979) 473–476.

[36] Y. Zhang, Q. Huo, P. Du, L. Wang, A. Zhang, Y. Song, Y. Lv, G. Li, Advances in new cathode material $LiFePO_4$ for lithium-ion batteries, Synth. Met. 162 (2012) 1315–1326.

[37] L. Wang, X. Zhou, Y. Guo, Synthesis and performance of carbon-coated $Li_3V_2(PO_4)_3$ cathode materials by a low temperature solid-state reaction, J. Power Sources. 195 (2010) 2844–2850.

[38] P. Fu, Y. Zhao, Y. Dong, X. An, G. Shen, Low temperature solid-state synthesis routine and mechanism for $Li_3V_2(PO_4)_3$ using LiF as lithium precursor, Electrochim. Acta. 52 (2006) 1003–1008.

[39] P. Fu, Y. Zhao, Y. Dong, X. An, G. Shen, Synthesis of $Li_3V_2(PO_4)_3$ with high performance by optimized solid-state synthesis routine, J. Power Sources. 162 (2006) 651–657.

[40] X. Rui, Q. Yan, M. Skyllas-Kazacos, T.M. Lim, $Li_3V_2(PO_4)_3$ cathode materials for lithium-ion batteries: A review, J. Power Sources. 258 (2014) 19–38. doi:10.1016/j.jpowsour.2014.01.126.

[41] B. Huang, X. Zheng, M. Lu, S. Dong, Y. Qiao, Novel Spherical $Li_3V_2(PO_4)_3$ Cathode Material for Application in High – Power Lithium Ion Battery, Int. J. Electrochem. Sci. 7 (2012) 437–444.

[42] A.F. Liu, Z.L. Yin, Electrochemical Performance of the $Li_3V_2(PO_4)_3$/C Synthesized from $V_2O_3$, Key Eng. Mater. 519 (2012) 142–146. doi:10.4028/www.scientific.net/KEM.519.142.

[43] D. Choi, P.N. Kumta, Surfactant based sol–gel approach to nanostructured $LiFePO_4$ for high rate Li-ion batteries, J. Power Sources. 163 (2007) 1064–1069.

[44] H. Liu, Y.P. Wu, E. Rahm, R. Holze, H.Q. Wu, Cathode materials for lithium ion batteries prepared by sol-gel methods, J. Solid State Electrochem. 8 (2004) 450–466.

[45] L.L. Hench, J.K. West, The sol-gel process, Chem. Rev. 90 (1990) 33–72.

[46] M.M. Ren, Z. Zhou, X.P. Gao, W.X. Peng, J.P. Wei, Core− shell $Li_3V_2(PO_4)_3$@C composites as cathode materials for lithium-ion batteries, J. Phys. Chem. C. 112 (2008) 5689–5693.

[47] A. Yamada, S.-C. Chung, K. Hinokuma, Optimized $LiFePO_4$ for lithium battery cathodes, J. Electrochem. Soc. 148 (2001) A224–A229.

[48] R. Dominko, M. Bele, M. Gaberscek, M. Remskar, D. Hanzel, S. Pejovnik, J. Jamnik, Impact of the carbon coating thickness on the electrochemical performance of $LiFePO_4$/C composites, J. Electrochem. Soc. 152 (2005) A607–A610.

[49] J. Barker, M.Y. Saidi, J.L. Swoyer, A carbothermal reduction method for the preparation of electroactive materials for lithium ion applications, J. Electrochem. Soc. 150 (2003) A684–A688.

[50] J. Barker, M.Y. Saidi, J.L. Swoyer, Electrochemical insertion properties of the novel lithium vanadium fluorophosphate, $LiVPO_4F$, J. Electrochem. Soc. 150 (2003) A1394–A1398.

[51] D.E. Newbury, N.W.M. Ritchie, Elemental mapping of microstructures by scanning electron microscopy-energy dispersive X-ray spectrometry (SEM-

EDS): Extraordinary advances with the silicon drift detector (SDD), J. Anal. At. Spectrom. 28 (2013) 973–988. doi:10.1039/c3ja50026h.

[52] W. Wang, H. Wang, S. Liu, J. Huang, Synthesis of γ-$LiV_2O_5$ nanorods as a high-performance cathode for Li ion battery, J. Solid State Electrochem. 16 (2012) 2555–2561.

[53] Z. Huang, L. Cao, L. Chen, Y. Kuang, H. Zhou, C. Fu, Z. Chen, Preparation, Characterization, and Lithium Intercalation Behavior of $LiVO_3$ Cathode Material for Lithium-Ion Batteries, J. Phys. Chem. C. 120 (2016) 3242–3249.

[54] G. Ali, A. Mehmood, H.Y. Ha, J. Kim, K.Y. Chung, Reduced graphene oxide as a stable and high-capacity cathode material for Na-ion batteries, Sci. Rep. 7 (2017) 40910.

[55] Q. Chen, J. Wang, Z. Tang, W. He, H. Shao, J. Zhang, Electrochemical performance of the carbon coated $Li_3V_2(PO_4)_3$ cathode material synthesized by a sol-gel method, Electrochim. Acta. 52 (2007) 5251–5257. doi:10.1016/j.electacta.2007.02.039.

[56] W.E. Moddeman, A.R. Burke, W.C. Bowling, D.S. Foose, Surface oxides of boron and $B_{12}O_2$ as determined by XPS, Surf. Interface Anal. 14 (1989) 224–232.

[57] B. Zhang, C. Shen, J. Zheng, Y. Han, J. Zhang, L. Ming, J. Wang, S. Qin, H. Li, Synthesis and Characterization of a Multi-Layer Core-Shell Composite Cathode Material $LiVOPO_4$- $Li_3V_2(PO_4)_3$, J. Electrochem. Soc. 161 (2014) A748–A752.

[58] E. Hryha, E. Rutqvist, L. Nyborg, Stoichiometric vanadium oxides studied by XPS, Surf. Interface Anal. 44 (2012) 1022–1025.

[59] G. Silversmit, D. Depla, H. Poelman, G.B. Marin, R. De Gryse, Determination of the V2p XPS binding energies for different vanadium oxidation states ($V^{5+}$ to $V^{0+}$), J. Electron Spectros. Relat. Phenomena. 135 (2004) 167–175.

[60] J. Mendialdua, R. Casanova, Y. Barbaux, XPS studies of $V_2O_5$, $V_6O_{13}$, $VO_2$ and $V_2O_3$, J. Electron Spectros. Relat. Phenomena. 71 (1995) 249–261.

[61] J. Światowska-Mrowiecka, V. Maurice, S. Zanna, L. Klein, P. Marcus, XPS study of Li ion intercalation in $V_2O_5$thin films prepared by thermal oxidation of vanadium metal, Electrochim. Acta. 52 (2007) 5644–5653.

[62] N. Dupré, J.F. Martin, D. Guyomard, A. Yamada, R. Kanno, Characterization of interphases appearing on $LiNi_{0.5}Mn_{0.5}O_2$ using $^7$Li MAS NMR, J. Power Sources. 189 (2009) 557–560.